IPST Technical Paper Series Number 514

The Cause and Effects of Perforations in a Liquid Sheet from a Splash-plate Spray Nozzle

T.M. Spielbauer and C.K. Aidun

February 1994

Submitted to
J. Liq. Atomization and Sprays

Submitted to: *J. Liq. Atomization and Sprays*

THE CAUSE AND EFFECTS OF PERFORATIONS IN A LIQUID SHEET FROM A SPLASH-PLATE SPRAY NOZZLE

Thomas M. Spielbauer
Senior Research Engineer
3M
3M Center 230-ID-28
St. Paul, MN

Cyrus K. Aidun
Associate Professor
Institute of Paper Science and Technology, and
School of Mechanical Engineering at
Georgia Institute of Technology
Atlanta, GA

Corresponding Author:

Cyrus K. Aidun
IPST/ME
Georgia Institute of Technology
500 10th Street, N.W.
Atlanta, Georgia, 30318-0620

Tel. (404) 853-9777
Fax. (404) 853-9510

e-mail: ipchmca@hydra.gatech.edu

ABSTRACT

The physical processes which can cause a radially thinning liquid sheet to rupture, including suspended solid particles, entrained air bubbles, drop impingement, and wave interactions, are evaluated with a simple splash plate nozzle. Relying on both experimental and analytical results, the importance of hydrodynamic mechanisms and rupture initiated by external effects are discussed. The influence of external vibrations on the wave disturbances and sheet breakup is also presented.

INTRODUCTION

This study focuses on the formation of drops from a simple, sheet producing nozzle. The device, called a splash plate nozzle, forms a liquid sheet by impinging a circular jet on a small, flat plate. The fluid spreads out on the plate and, when it reaches the edge, continues to expand radially forming a free thin sheet. Although experiments were conducted using this single design, the qualitative and analytical descriptions of sheet breakup developed are expected to apply to a variety of sheet producing devices.

It is convenient to separate the description of the spraying process into three stages: (1) the formation of a thin sheet of liquid, (2) the breakup of this sheet into cylindrical strands, and (3) the disintegration of these strands into drops. The potential variability of the fundamental processes occurring in each of these steps may contribute to the production of the distribution of drop sizes observed experimentally, and each stage will be examined in turn.

A vast array of nozzle designs are available for the production of liquid sheets. Masters[1] has presented an overview of the nozzles commonly used in spray drying applications. Lefebvre[2,3] has reviewed the mechanisms of atomization, the flow characteristics, and the

performance of a variety of nozzle designs, focussing on those used in combustion applications. In the study to be discussed here, a simple splash plate nozzle was analyzed in some detail.

A splash plate nozzle is shown in Fig. 1. In this nozzle, the liquid is accelerated through a short entrance length tube and exits from a circular orifice. The resulting free jet travels a short distance before striking a flat plate. The forces developed in the region of impact drive the liquid out radially, nearly parallel to the plate surface.[4]

Taylor performed several studies on the formation of sheets either by the impingement of two opposing jets[5] or by the impingement of a single jet on a plate.[4,6,7] For the case of a jet impinging on a plate at a 90° angle, a mass balance can be used to predict the sheet thickness as a function of the distance downstream. Such an expression was reported by Taylor[7] and, after a change of variables, is given here as

$$2h(x) = \left(\frac{d_0^2}{8x}\right)\left[\frac{U_0}{U_{s,avg}(x)}\right], \tag{1}$$

where: d_0 = nozzle orifice diameter;

h = sheet half-thickness ($2h$ = full thickness of the sheet);

U_0 = jet velocity;

$U_{s,avg}$ = average sheet velocity; and

x = radial position downstream from the point of jet impact.

In this expression, $2h$ rather than h is used to represent the sheet thickness in order to be consistent with the nomenclature used in derivations to be presented below.

It can be seen from Eq. 1 that the downstream sheet thickness is affected by two independent processes. First, the sheet thins due to the radial spreading of the fluid. This is a purely geometrical effect and is expressed as $d_0^2/8x$. If there were no momentum losses in the region of jet impact, and the fluid was inviscid such that no momentum loss occurred due to

viscous shear at the plate surface, then the sheet thickness as a function of radial position would be described by this term alone. The inviscid sheet thickness is shown as a dashed line in Fig. 1.

Losses are expected to occur in all real spray systems. The resulting decrease in fluid momentum is accounted for by the second term in Eq. 1, $U_0/U_{s,avg}(x)$, since any loss in momentum of the fluid will result in a decrease in the average sheet velocity relative to the jet velocity. The average sheet velocity is expressed as a function of x because viscous shear forces at the plate surface are expected to decrease the fluid momentum continuously as the fluid expands radially on the plate. The thickness of viscous fluid spreading on a plate is shown as a solid line in Fig. 1.

Although Taylor[7] did not identify the nature of the losses he observed, he estimated the decrease in velocity to be 20%, so that he reported a constant value for $U_0/U_{s,avg}$ of 1/0.8.

Watson[8] also derived an expression relating the thickness to the downstream position for a liquid expanding radially on a solid surface. Only viscous shear losses were considered in the calculation of the sheet velocity. In this analysis, a similarity solution based on either a developing or fully developed boundary layer was used. The radial component of velocity was expressed as

$$U(x,z) = U_{max}(x) \cdot f(z/2h). \tag{2}$$

In this expression, $U_{max}(x)$ is the maximum sheet velocity and is a function of the radial position measured downstream from the point of jet impact, only. The similarity function, $f(z/2h)$, was determined as part of Watson's analysis.

The location of the transition from the developing boundary layer region to the fully developed boundary layer region, x_t, was defined by Watson as

$$x_t = 0.1834 d_0 \cdot Re_{jet}^{1/3}, \tag{3}$$

where the jet Reynolds number, Re_{jet} is defined as $\rho_{liq} U_0 d_0 / \mu_{liq}$. The numerical constant in Eq. 3 differs from that reported by Watson due to differences in the definition of the characteristic length scale.

As the radial location increases from x to x_t, the boundary layer thickness, δ, increases from 0 to $2h(x)$. The fluid above the boundary layer $(\delta \le z \le 2h[x])$ is assumed to be unaffected by the shear forces and maintains a velocity equal to that of the incident jet. The boundary layer thickness increases with x until the fluid passes into the region $x > x_t$. At this point the boundary layer thickness is equal to the sheet thickness; the unaffected fluid region no longer exists; and the top surface velocity begins to decrease.

Huang[9] investigated the breakup length of sheets at higher Weber numbers as well $800 < We_{jet} < 30,000$. He shows that in contrast to the case when $We_{jet} < 800$ where the breakup distance is determined by the balance of surface tension and inertial forces, when $We_{jet} > 800$ the presence of large amplitude antisymmetric waves result in the destruction of the sheet before the equilibrium position is attained. Thus, for circular sheets produced in this range of Weber numbers, the rim disintegration mechanism is not expected to contribute to the formation of drops.

The waves observed by Huang[9] were described qualitatively by Dombrowski and Fraser.[10] They noted that a wave mechanism of liquid sheet breakup occurred at conditions of low viscosity and low surface tension. The waves were induced by aerodynamic forces acting on the air/liquid interface. As the amplitude of the waves increased, strands were torn from the crests, and holes were blown through the sheet. The holes formed in this manner were characterized by the shedding of drops from their expanding rims.

Fraser et al.[11] described an idealized wave disintegration mechanism which is summarized here. A single, optimally growing wave increases in amplitude with position downstream. When this wave reaches its critical amplitude, sheet segments are torn off at half-wavelength intervals to form bands of liquid. Surface tension forces rapidly contract these bands into cylindrical strands which ultimately break up into drops.

Analyses of the wave breakup mechanism have focused on the temporal or spatial growth of disturbances to the air/liquid interface. When this boundary is perturbed, aerodynamic, inertial, surface tension and viscous forces will be active. The stability of the sheet and the growth rate of unstable disturbances are determined by the relative magnitudes of these forces.

Li and Tankin[12] analyzed the stability of viscous sheets over a wide range of Weber numbers. In agreement with Dombrowski and Johns,[13] they found that an increase in liquid viscosity reduced the growth rate of aerodynamic instabilities and increased the wavelength of maximum growth rate. In addition to the aerodynamic instability, they reported the existence of a viscosity-enhanced instability. However, this mechanism was only important when the gas phase Weber number was less than the ratio of gas density to liquid density.

Dombrowski and Johns[13] considered the stability of a sheet that decreased in thickness with position downstream; however, they assumed that the rate of change of sheet thickness was small enough that the sheet could be modeled as planar at any given location. Weihs[14] also examined the behavior of radially thinning, viscous sheets, but did not apply the local planar sheet assumption in his initial analysis. Both Weihs[14] and Dombrowski and Johns[13] determined that the temporal instability limit was identical to that predicted by Fraser et al.[11] and Hagerty and Shea,[15] and that the wave of maximum growth rate was a function of sheet velocity and thickness. The magnitude of the change in the wavelength of maximum growth rate per unit change in sheet thickness was predicted to increase with increasing liquid viscosity.

In addition to the temporal instability reported by others, Weihs[14] predicted a form of spatial instability resulting from a sinusoidal disturbance with increasing successive maxima. This form of instability could occur even when the sheet was temporally stable.

The perforation mechanism has been investigated by numerous researchers. The source of the perforations has been attributed to a variety of causes including dissolved air, suspended particles, particle impingement, and others. Many of these mechanisms are particular to the specific operating conditions employed.

Fraser et al.[11] investigated the role of dissolved air in the formation of perforations. They obtained photographs of a water sheet produced by a fan spray nozzle. The sheet was formed in a vacuum in order to suppress aerodynamically-induced waves. Both aerated and deaerated distilled water sheets were examined. The air content was reported to have no effect on the formation of holes nor on the breakup length of the sheet.

Clark and Dombrowski[16] also investigated the role of the release of dissolved air on hole formation. They sprayed tap water, which was found to be supersaturated with air, and distilled water with the air content reduced to 1 p.p.m. At conditions when perforations were formed, no difference in the breakup of the sheets could be detected.

Dombrowski and Fraser[10] studied the breakup of water and alcohol sheets containing 3-60 micron suspended solid particles. Regardless of their size, particles wetted by the liquid did not lead to the formation of holes. Particles which were not wetted, however, initiated a perforation when the thickness of the sheet was on the order of the characteristic particle dimension.

Similarly, a water/oil emulsion spray was observed to break up via the perforation mechanism.[10] As the oil globule size was increased, the sheet ruptured closer to the nozzle where the sheet was thicker, and the breakup length of the sheet decreased.

Fraser et al.[11] observed local disturbances on liquid sheets. They reported that, while not all such disturbances developed into perforations, all perforations resulted from this source. The local disturbances were attributed to the impingement of particles on the sheet surface. These particles were assumed to be drops of the sprayed liquid, and their source was investigated.

Fraser et al.[11] reported that the number of perforations was not reduced when the position of baffles in the spray chamber were adjusted to protect the sheet from drops deflected from the walls nor were perforations eliminated by the placement of parallel glass plates close to, and on opposite sides of the sheet. It was concluded that the drops must form at the nozzle tip and follow a trajectory close to the sheet before striking it. The entrainment of ambient air by the high velocity liquid sheet was suggested as the mechanism causing drops to follow such a path.

Clark and Dombrowski[16] investigated the breakup of liquid sheets formed in a high temperature environment. They observed two distinct wave disturbances on the sheet. The first type, observed at low ambient temperatures, was simply the aerodynamic waves discussed previously. The second type was only observed at high ambient gas temperatures. The wavelengths of these disturbances were much shorter than the lower cutoff limit predicted for aerodynamically-induced waves. These second waves, reported to be electrohydrodynamic in origin, were symmetric, suggesting that local thin spots led to the formation of perforations.

The fluid contained in a thin liquid film possesses different thermodynamic properties than does the same fluid in a bulk phase.[17] Short-range forces such as electric double layer interaction and London dispersion forces affect the stability of such films.

Patzer and Homsey[18] performed a theoretical analysis on the stability of spherically concentric, draining, fluid sheets. They predicted a critical film thickness for rupture on the order of one micron. This value is expected to be an upper bound, as the stabilizing effects of electric double layer repulsion were neglected.

Pandit and Davidson[19] studied the rupture of thin, draining spherical films experimentally. They found a critical rupture thickness of 0.05-0.09 microns. High ionic strength salts were added to the liquids in sufficient concentration to suppress the effects of the electric double layer; thus, these values may be considered an upper bound for the spontaneous rupture thickness, as well.

Point disturbances were observed by Dombrowski and Fraser.[10] These disturbances were shown to have originated at the nozzle orifice and were believed to be the result of turbulence. However, spontaneous rupture was ruled out as the source of perforations.

Once a hole is formed in a liquid sheet, its stability will be determined by the balance of force acting upon it. Taylor and Michael[20] calculated, that for a planar sheet in equilibrium, any hole with a radius greater than the thickness of the liquid sheet would grow, while smaller holes would close. This conclusion was based on minimizing the surface area. Experiments in which a hole was formed in a sheet of mercury suspended in water demonstrated the existence of a minimum initial hole size for growth to occur.

Fraser et al.[11] calculated the growth rate of perforations in a flat sheet by balancing surface tension and inertial forces. The resulting expression is given as

$$e = \frac{\partial R_p}{\partial t} = \sqrt{\frac{\sigma}{h\rho_{liq}}}, \tag{4}$$

where: e = growth rate of a perforation; and
R_p = radius of a perforation.

In order to maintain a nomenclature consistent with that used to describe the wave mechanism, the symbol h is used to designate the half-thickness of the sheet. For the case of a radially thinning liquid sheet, the half-thickness is inversely proportional to the downstream position.

If the rate of change in sheet thickness is small, as it is far from the nozzle orifice, then the value of h in Eq. 4 can be taken as the half-thickness of the sheet at the center of the perforation as given by

$$h = \frac{K_N}{x}. \tag{5}$$

The proportionality constant, K_N, is a function of the nozzle geometry and the flow characteristics of the sheet. The expression for perforation growth rate in a thinning sheet is then

$$e = \sqrt{\frac{\sigma x}{\rho_{liq} K_N}}. \tag{6}$$

Fraser et al.[11] found good agreement between perforation growth rates predicted with this expression to those measured experimentally.

The purpose of this study is to investigate the breakup mechanisms which dominate the disintegration of thin liquid sheets. Because of the complex flow characteristics of industrial nozzles, a simple spray configuration will be used. The particular geometry and flow characteristics were selected to be similar to those of an idealized spray device, the splash plate nozzle. It is expected that the results obtained using this nozzle will apply in varying degrees to other sheet forming devices as well.

EXPERIMENTAL APPROACH

The main objective of this study is to determine the dominant mechanisms of breakup for splash plate sprays. The mechanisms of sheet disintegration can be identified only by observing the spraying process; therefore, a facility was constructed to produce and allow the imaging of splash plate sprays. The process equipment used to produce the liquid sheet and to monitor the relevant parameters are described below.

Because of the high liquid velocities, neither direct observation nor standard photographic procedures can be used to examine sheet behavior; therefore, a variety of alternative imaging techniques were employed. The imaging methods used were short duration, intensified video imaging' and high-speed 16 mm silver halide film photography.

THE SPRAY FACILITY

A sketch of the spray facility used in this study is shown in Fig. 2. A 1.2 m x 1.2 m (4 ft. x 4 ft.) galvanized steel tank acts as a reservoir for the test fluid. The bottom of the tank slopes toward a drain located in the center of the base, providing 380 liters (100 gallons) of storage capacity. Plexiglass walls extend upward on all four sides to constrain the spray. These transparent walls provide flexibility in locating the lighting sources needed to image the sprays. A 0.5 m x 0.5 m (20 in. x 20 in.) Plexiglass window installed in the bottom of the tank allows the spray to be illuminated from below, as well.

The outlet of the tank discharges to the inlet of a Roper 2AM06 rotary gear pump. This pump is rated to deliver 0.023 liters (0.006 gallons) per revolution with a maximum discharge pressure of 890 kPa (100 psi). A 3.0 hp, 1725 RPM motor drives the pump, thus delivering a constant flow rate of approximately 40 liters/min (10 gallons/minute).

The discharge from the pump splits into two 1½ inch internal diameter (I.D.) lines. One line, a short recirculation loop, discharges back into the reservoir. A ball valve located in this loop controls the relative flow rates through the two lines. The main line reduces to a one inch nominal I.D. pipe before connecting to a viscometer and a flowmeter in series. The pipe reduces to one-half inch before entering a flexible tube installed to dampen any vibrations in the system. The flexible line connects to a 90° elbow, and the liquid then flows through a 56 cm (22 inch) one-half inch schedule 40 pipe (1.58 cm, 0.655 inch I.D.). A collar, located at the discharge end of this straight length of pipe, connects the nozzle to the main flow loop.

The in-line viscometer is a Brookfield TT100 coaxial cylinder rotational viscometer. The rotational speed of the sensing element is 72 RPM. The viscometer was calibrated to achieve a reported accuracy of 1% of full scale. The full-scale range used was 0-200 cp, leading to a bias error of ± 2 cp.

A Smith Meter Inc. S100 S-mass meter was used to obtain mass flow rate and density information. For the flow rate, a rated accuracy of ±0.15% of full scale was calculated for the operating conditions employed. This corresponds to a bias error of ±0.3 kilograms per minute (±0.6 pounds per minute). The reported accuracy of the density output of the S-mass meter is ±0.005 g/cm^3.

An Omega type J thermocouple was installed through the elbow upstream of the nozzle. The thermocouple tip was centered in the vertical pipe length about 2 cm (1 inch) downstream of the elbow. The analog output from the thermocouple was processed by an Omega model #650J-A digital thermometer. Accounting for the uncertainty in the thermocouple and the digital thermometer, the bias error in the temperature measurements is ±2°C.

A flush mounted pressure transducer (Sensotec model #Z/5541-07) is connected to a Sensotec Model GM signal condition-indicator. The bias error in the pressure measurements resulting from this combination is ±0.3 psia.

A threaded support rod, welded to the base of the tank directly below the discharge orifice of the nozzle, provides support for a stainless steel plate 4.99 cm (1.96 inches) in diameter. Positioning rods connected the support rod to four equally spaced locations on the base of the reservoir. Using these positioning rods, the support rod can be adjusted to ensure that the plate's surface is horizontal. Because the plate was mounted in the center of the reservoir, the liquid sheet formed from the impact of the jet on the plate will travel a minimum distance of 0.6 m (2 ft.) before striking the Plexiglass walls encompassing the spray chamber.

The top and side surfaces of the plate were polished with progressively finer grades of sandpaper. Following the polishing procedure, the surfaces of the plate were treated with a silicone release agent. The procedure for polishing and coating the plates is outlined elsewhere (Spielbauer, 1993).[21]

Seven nozzles were used to produce straight jets. The orifice diameter of each nozzle was measured using a telescope gage. The reported diameter is the average of four measurements made at equally spaced locations around the orifice. All of the nozzles were selected to mate with a 1/2" nominal female pipe connection. The entrance region, where the flow area decreased from the 1/2" pipe to the final orifice dimension, varied with nozzle design, as sketched in Fig. 3.

Table 1. Straight jet nozzle descriptions.

nozzle	nominal diameter	measured diameter
[a]Bete Fog NF-6000	3/16 inch (4.76 mm)	4.83 ± 0.01 mm
Bete Fog NF-8000	7/32 inch (5.56 mm)	5.56 ± 0.02 mm
Bete Fog NF-10000	1/4 inch (6.35 mm)	6.07 ± 0.01 mm
[b]S.S. Co. QU-00100	15/64 inch (5.95 mm)	5.94 ± 0.01 mm
S.S. Co. QU-00120	1/4 inch (6.35 mm)	6.56 ± 0.01 mm
S.S. Co. QU-00200	21/64 inch (8.33 mm)	8.45 ± 0.01 mm
Sharp Edge	1/4 inch (6.35 mm)	6.36 ± 0.02 mm

a Bete Fog Inc., Greenfield, MA 01302

b Spraying Systems Co., Wheaton, IL 60188

The location of the nozzle relative to the plate was controlled by four positioners used to connect the movable vertical pipe, to which the nozzle was attached, to the rigid support structure mounted around the spray tank. A Newport TSV-9 vertical positioner was used to raise and lower the nozzle relative to the fixed plate surface. A Newport 460-XZ positioner was used to locate the nozzle in the plane perpendicular to the vertical axis such that the jet impacted at the center of the plate. Finally, two Newport 481-S rotary stages were used to ensure that the angle of jet impact relative to the plate surface was 90°.

Sheet thickness probes, in the form of three extended micrometers, were installed around the nozzle, 120° apart. The location of each micrometer tip was 2.14 ± 0.04 cm (0.84 ±0.03 inch) downstream from the center of jet impact and, thus, 0.36 ± 0.04 cm upstream from the edge of the plate.

The in-line data acquisition devices (viscometer, flow and density meter, thermocouple, and pressure transducer) were connected to the Metrabyte DAS-8PGA analog to digital data conversion system. The data were collected using LABTECH NOTEBOOK installed on a PC.

The surface tension of the fluid, glycerol/water solution, was measured off-line using a DuNouy ring tensiometer.

In order to examine the mechanisms of breakup, the images obtained must effectively freeze the motion of the spray. Motion blur is defined as the distance an object moves during the time it is being imaged (the exposure time). Depending on the field of view and the intended end-use of the images, a motion blur of less than 0.1 to 1.0 mm was desired. Sheet velocities on the order of 10 m/s were expected; therefore, the maximum imaging time allowable was 10-100 μsec.

A Xybion ISG-500 intensified gated camera was used to obtain images of the spray stored directly on super VHS videotape for later analysis. This camera had a fixed imaging rate of 30 frames per second; however, the exposure time for each image can be adjusted continuously between 25 nanoseconds and 30 milliseconds ($25 \times 10^{-9} \leq t \leq 30 \times 10^{-3}$ seconds).

A Redlake Hycam 16 mm high-speed camera was also used to obtain spray images. This rotating prism camera is capable of shuttering rates up to 10,000 frames per second. The exposure time for each frame is equal to (1/2.5) divided by the framing rate. Kodak 3-X and 4-X reversal film was used to collect the images. When processed, this film yields positive prints of the subject, directly.

The imaging rate of the Hycam is not constant throughout a given run, but rather, an acceleration period is followed by a constant imaging rate period. In order to determine the framing rate at each position on the exposed film, a built-in timing light generator (TLG) was

used. This device places marks on the periphery of the film at a user selected rate of 100, 1000, or 5000 hertz with a reported accuracy of 0.01%. After exposing the film, the number of marks per frame could be counted. Then, using the known TLG rate, the framing rate could be determined.

RESULTS

MECHANISM OF SHEET BREAKUP

The photographs shown as Figs. 4-7 represent only a small fraction of the high-speed 16 mm and video images obtained in this study. After reviewing the full set of films obtained, a qualitative description of the breakup process was developed with the aid of theoretical analyses.

The formation and interaction of holes in the sheet clearly dominate the first stage of sheet breakup. The majority of these holes form in a narrow region of the downstream position. These holes grow rapidly, interact to form clumps and strands of liquid which ultimately break up into drops.

The formation and growth of a perforation is shown in Figs. 4a-l. The rim of the perforation is first visible in Fig. 4c. If the hole is present in the prior images, the resolution of the images is not sufficient to detect it. In subsequent images (4d-l), the perforation grows, and its rim becomes thicker. In Figs. 4j-l, the perforation rim approaches and ultimately merges with the rims of other perforations, forming a small network of strands.

The interaction of two adjacent perforations is also shown in Figs. 5a-f. In Fig 5b, a section of the sheet is seen inside the perimeter of the lower perforation. This indicates that the

sheet is folding over upon itself, as the visible sheet segment is below the region containing the perforation.

Figure 6 shows a section of the sheet in the region of breakup. The light streaks in the upper right-hand corner are associated with the sinuous waves in the sheet. A spray of droplets can be seen in the lower left-hand corner of the image. The transition from the sinuously disturbed sheet to the droplets is seen to occur in a narrow band, approximately 2-3 cm wide. In this region, the merging of several perforations and the resulting formation of clumps and strands can be seen.

Using a procedure to be described in detail in a later section, the radially expanding sheet was split with a thin wire. Downstream from the split, surface tension forces contract the fluid into rims as described previously. These rims were illuminated with a strobe light and imaged. One such image is shown in Fig. 7a. A sinuous wave disturbance is clearly visible from the point at which the sheet is split (near the right-hand side of the image) out to the region of breakup (near the left-hand side of the image). The narrow range over which the liquid progresses from a sinuously disturbed sheet to a spray of drops should be noted in this picture as well.

A second image of the rims formed by splitting the sheet is shown in Fig. 7b. Again, sinuous waves are visible. This wave is seen to grow with position downstream (from right to left) and becomes distorted from a pure sine wave.

These images, showing the growing sinuous waves, the distortion of the waves as their amplitude increases, the folding over of the sheet, the formation and growth of perforations, the interaction of neighboring perforation rims to form clumps and strands, and the breakup of these clumps to form drops, demonstrate the complexity of the overall drop formation process. In

order to increase our understanding of this process, certain aspects of the breakup of liquid sheets were investigated in greater detail.

LOCATION OF SHEET RUPTURE

As discussed in the previous section, although perforations were observed throughout the length of the sheet, the majority of the holes appeared in a narrow region near the point of breakup. Experiments were performed to quantify the radial distribution of perforations as a function of the nozzle diameter and the jet velocity.

Liquid sheets were formed by the perpendicular impingement of a circular jet on a polished disc. The jet diameter was varied by using three nozzles with different orifice sizes. Each nozzle was operated over its practical range of jet velocities using a glycerol/water solution as the test liquid. The Xybion high-speed video camera was focused on a small area of the sheet, downstream from the plate edge. Images were collected for approximately one minute; thus, as the Xybion operates at a rate of 30 frames per second, about 2000 images were obtained during each trial. This process was repeated at a series of downstream positions. One thousand images were viewed for each combination of nozzle diameter, jet velocity, and downstream location. The perforations observed in these images were counted, and the size and scale of the images were recorded. For details see Spielbauer[21].

Because the imaging area was independent of the downstream location, the fraction of the total circumferential area of the spray observed varied with the radial position. Therefore, to provide a uniform basis for comparison, the observed perforation counts were normalized. The area corrected perforation count, $(Np)_{area}$, was obtained by first multiplying the number of perforations observed, $(Np)_{obs}$, by the ratio of the circumference of the spray sheet at the imaging

position, x, to the width of the imaging area, W. This value was then divided by the radial span of the imaging area, S, to obtain

$$(Np)_{area} = (Np)_{obs} \cdot \left(\frac{2\pi x}{WS}\right), \tag{7}$$

where:
- x = radial position of the center of the imaging area;
- $(Np)_{obs}$ = number of perforations observed at downstream position, x;
- $(Np)_{area}$ = area corrected number of perforations at downstream position per radial span;
- W = lateral width of the imaging area; and
- S = radial span of the imaging area.

The width and span are defined in Fig. 8 for two representative locations.

In order to estimate the number of <u>new</u> perforations formed in a given range of downstream position, the area corrected perforation count at each location was modified to exclude the perforations accounted for at positions upstream of that location. Thus, if the sheet is imaged at some number of radial positions, M, then the number of perforations reported for the m^{th} position (where $2 \le m \le M$) is given by

$$(Np)_{rep,m} = (Np)_{area,m} - \sum_{j=1}^{m-1} (Np)_{rep,j}, \quad (\text{for } m \ge 2). \tag{8}$$

The range of parameters investigated in this set of experiments is summarized in Table 2. A complete list of the operating conditions, including the observed and the normalized perforation counts, is included in Appendix C of Spielbauer[21].

Table 2. Operating conditions for the radial perforation distribution experiments.

nozzle	number of trials	number of locations	range of locations (cm)	range of jet velocities (m/s)
NF-6000	22	5	13-21	15-20
NF-8000	38	7	8-21	12.5-22.5
NF-10000	16	3	10-20	12.5-22.5

The radial perforation distribution as a function of the jet velocity is shown for the three nozzle orifice diameters in Figs. 9-11. The reproducibility of these experiments can be estimated by comparing the data presented for duplicate runs performed at 19 cm downstream with the NF-6000 nozzle (labeled as 19a and 19b in Fig. 9) and duplicate runs at 16 cm downstream for the NF-8000 nozzle (labeled 16a and 16b in Fig. 10). As can be seen in these plots, only a small percentage of the total number of perforations observed occurred in the region near the splash plate ($x < \approx 16$ cm). This relatively undisturbed portion of the spray was followed by a narrow band of downstream positions in which a rapid increase in the number of observed perforations was recorded. The downstream location at which this transition occurred varied with the orifice diameter and the jet velocity. In general, the downstream location at which the rapid increase in observed perforations occurred decreased with increasing jet velocity.

In each of the three plots showing the number of perforations recorded, no data are plotted for the trials corresponding to the highest jet velocities and furthest positions downstream. These trials were run, and the high-speed video images were reviewed; however, in these cases the sheet had already broken up into clumps and strands, and a numeric value for the number of perforations could not be determined accurately.

The thickness and the velocity of a free sheet affect both the wave and perforation mechanisms of breakup; thus, it would be advantageous to be able to predict these parameters as

functions of the operating conditions and fluid properties, particularly in the region of rapid perforation.

The expressions for the downstream sheet thickness in the developing and fully-developed boundary layer regions are based on the work by Watson with detailed derivations given in Spielbauer and Aidun[24]. These expressions can be divided through by the theoretical inviscid half-sheet thickness, h*, in order to obtain an equation for predicting the velocity or sheet thickness ratio. The expression obtained for the developing boundary layer region $(x \le x_t)$ is

$$\frac{h}{h^*} = \frac{U_0}{U_{s,avg}} = 1.0 + \frac{7.96}{(Re_{jet})^{1/2}} \left(\frac{x}{d_0} \right)^{3/2}, \tag{9}$$

and the equation for the fully-developed boundary layer region $(x > x_t)$ is

$$\frac{h}{h^*} = \frac{U_0}{U_{s,avg}} = 1.39 + \frac{38.7}{Re_{jet}} \left(\frac{x}{d_0} \right)^3. \tag{10}$$

Where the inviscid downstream sheet thickness is given by

$$2h^* = \frac{d_0^2}{8x}. \tag{11}$$

Once the liquid leaves the plate surface at x_p a simple mass balance can be used to predict the decrease in the sheet thickness with downstream position. The mass balance can then be written as

$$[2\pi x][2h(x)]U_{s,avg}(x) = [2\pi x_p][2h(x_p)]U_{s,avg}(x_p). \tag{12}$$

If the downstream sheet velocity is assumed to be equal to the average sheet velocity at the plate edge $\left(U_{s,avg}[x] = U_{s,avg}[x_p]\right)$, then this expression can be reduced to

$$h(x) = h(x_p) \cdot \left(\frac{x_p}{x}\right). \tag{13}$$

The thickness of the liquid sheet at the edge of the splash plate can be estimated, and Eq. 13 can then be used to estimate the sheet thickness at any position, $x > x_p$ as shown in Spielbauer and Aidun[23].

In the perforation distribution experiments, the sheet thickness on the plate edge was found to vary from 400 to 700 microns. Using Eq. 13 and the measured radius of the plate (x_p = 2.54 cm), the decrease in sheet thickness with downstream position was determined. These calculated results are plotted in Fig. 12 for the range of sheet thicknesses at the plate edge observed experimentally.

Because the sheet thickness at the plate edge varies with the jet velocity, the fluid properties, and the orifice diameter the sheet thickness variation with downstream location was calculated for each individual perforation count experiment. The number of perforations observed for each trial, previously plotted versus downstream location in Figs. 9-11, is now plotted versus the predicted sheet thickness in Fig. 13. Although there is significant scatter in the data, there appears to be a critical range for sheet thicknesses in which the majority of the perforations occur.

Several trends in the breakup behavior can be inferred from the qualitative features observed in Figs. 9-11 and Fig. 13. First, from Fig. 13, the sheet thickness at breakup is greater for the larger orifice diameter nozzle than for the smaller nozzles. This trend is also noted in Figs. 9-11, where for a fixed velocity, the number of perforations is seen to increase rapidly

closer to the plate as the orifice diameter is increased. Also, the number of perforations observed at a fixed position downstream increased with increasing velocity. These trends noted in the experimental data will be compared to results predicted from additional analyses of the breakup process.

WAVE THINNING

Although the perforation count versus sheet thickness data can be used to infer that a critical thickness for sheet rupture exists, as can be seen in Fig. 12, the sheet thickness is 100-130 microns in the breakup region. This is two to three orders of magnitude larger than the predicted critical sheet thickness for spontaneous rupture.[18,19] Also, as determined from analysis of variance, the critical sheet thickness may be affected by the orifice diameter and jet velocity. In order to address these issues, the investigation of the relationship between the downstream position, the sheet thickness, and the number of observed perforations was extended.

The sheet thickness values plotted in Fig. 12 were determined for systems free from external disturbances and will be referred to as the undisturbed sheet thicknesses. Sinuous and dilational waves are expected to disturb the planar geometry of the liquid sheet and, as will be shown, can reduce the thickness of the sheet.

Weihs[14] derived the relationship between the temporal growth rate parameter and the wave number of a sinuous disturbance in a viscous planar sheet. The expression he obtained is given here as

$$s_{imag} = \frac{vk^2}{2}\left[-1+\left(1+\frac{8\left(\rho_{gas}U_s^2k-\sigma k^2\right)}{2h\rho_{liq}v^2k^4}\right)^{1/2}\right]. \qquad (14)$$

The optimum wave number (i.e., wave length with maximum growth) can be obtained by differentiating this relation with respect to k, setting the result equal to zero and solving the resulting algebraic equation given by Spielbauer and Aidun[24]

$$k^{*3} - 4\Omega k^{*2} + 8\Omega k^{*} - 4\Omega = 0. \tag{15}$$

Here k* is a dimensionless wave number defined as the ratio of the wave number to the wave number of optimum growth in an inviscid sheet, given by

$$k^{*} = \frac{k}{k_{opt,inv}} = \frac{2\sigma k}{\rho_{liq} U_s^2}, \tag{16}$$

and the second dimensionless parameter, Ω, is defined by

$$\Omega = \frac{\sigma^3 \rho_{liq}}{\mu_{liq}^2 h \rho_{gas}^2 U_s^4}. \tag{17}$$

The operating conditions and fluid properties encountered in spray applications vary such that Ω can range over several orders of magnitude. At high values of Ω ($\Omega > 400$), k* is relatively insensitive to changes in Ω, while for intermediate values of Ω ($0.01 < \Omega < 400$), k* decreases significantly with a decrease in the log of Ω.

Once the sheet is formed, the only parameter in Ω which varies is the sheet thickness. The geometry of the nozzle can be used to determine the rate of change of sheet thickness with position downstream. This information can be used with the definition of Ω and its influence on k* to determine the expected variation in the wave number of optimum growth with position downstream.

The dominant wavelength has been measured from images of the side edges of sheets.[11,15,22] Because the sheet formed in this study had no side edges, the spray was split in

order to form them. When the sheet was split, the fluid near the newly formed edges contracted to form thick, visible rims. When the spray was then illuminated, the waves in the sheet could be examined by imaging the motion of the rims. Although splitting the sheet and the resultant formation of rims will alter the wave characteristics, this technique is expected to yield an estimate of the disturbance wavelengths.

The sheet was split by inserting a 0.030 inch diameter wire through the sheet, perpendicular to the direction of flow and the plane of the sheet. Provided the wire intersected the sheet far enough downstream, the sheet would split, and two rims would form. If the wire split the sheet too far upstream, the sheet would separate at the wire, but reconnect a short distance downstream. The position downstream at which the wire could be located and the sheet would stay separated increased with decreasing sheet velocity.

The spray was illuminated from below using a General Radio Company Strobtac 1531-A strobe light. The strobe frequency was adjusted for each trial in an attempt to freeze the motion of the waves. If the strobe frequency was too high, the waves appeared to move upstream, while if the strobe frequency was too low, they appeared to travel downstream. Images of the rims were collected using a 35 mm camera with ASA 1600 color slide film. Two examples of the images obtained were shown as Figs. 7a and 7b. In addition to the rim images, several images of a ruler, positioned next to the rim, were collected. These images were used as a reference scale for determining the disturbance wavelengths.

The slides were projected onto a sheet of paper, the rims were traced, and the wavelengths measured. The measured wavelengths are plotted versus the optimum inviscid wavelength in Fig. 14. The sheet velocity used to calculate the optimum disturbance wavelength was the arithmetic average velocity based on the two-term linear regression equation. The line of 1:1 correspondence between the predicted and measured wavelengths is shown as a solid line. A

second line shows the predicted wavelengths if the root mean square velocity based on the two-term linear regression equation is used. Although there is considerable scatter in measured wavelength data, good agreement between the predicted and measured wavelengths is shown.

External Disturbances

Experimental Measurements

Because the dominant wave may be related to vibrations in the spray system, these disturbances were investigated. An Endevco Model # 2217 accelerometer was used in conjunction with a Columbia Research Laboratories Inc., Model 4101 charge follower to monitor the vibrations in the system. The signal from the charge follower was collected with a LeCroy 7200 Precision Digital Oscilloscope. A fast Fourier transform (FFT) was used to convert the signal from the time domain into the frequency domain. The resulting FFT spectra were used to determine the dominant disturbance frequencies in the system.

Spectra were collected for the flowmeter, the viscometer, the pump, and the motor. In these trials, the accelerometer was held against the device being monitored by hand. The accelerometer was then mounted beneath the plate perpendicular to the plate surface. For these tests, a threaded hole was drilled in the base of the plate, 1/32" from the outer edge. The accelerometer could then be attached firmly to the plate using the screw provided with it.

A spectrum was obtained with all of the equipment associated with the spray apparatus turned off. Next, a spectrum was collected with the pump on, recirculating flow back to the reservoir (that is, no flow through the nozzle). FFT spectra were then collected while a jet of glycerol/ water was impinging on the plate. The jets were formed over a range of flow rates (11.7-21.9 m/s) using a QU-00120 nozzle. Finally, the disturbances to the nozzle at flow rates of

7.9 and 17.3 m/s were monitored. The accelerometer was held against the nozzle by hand during these tests. These spectra are included in Appendix J of (Spielbauer, 1993).[21]

There is a dominant peak at about 352 hertz in the FFT spectra for both the plate and the nozzle, independent of the jet velocity. The plate spectra has additional peaks, corresponding to several harmonics of the 352 hertz peak. These peaks can be seen in the plate spectrum for the 21.9 m/s flow rate shown in Fig. 15.

The 352 hertz peak may be related to a corresponding peak in the spectrum obtained for the motor driving the pump. Other frequencies associated with the pump, motor, or the data acquisition devices did not appear to affect the nozzle nor the plate.

In order to investigate the vibrations in the plane of the plate surface, a second mounting hole was drilled in the plate. This hole was located on the side of the plate, at the midpoint of the plate height. Four spectra were collected with the accelerometer mounted in the first hole (beneath the plate) in order to determine if the presence of the second hole altered the dominant frequencies. In all cases, a jet of glycerol/water was impinging on the plate. Seven spectra were then collected during jet impingement with the accelerometer mounted in the second hole, thus measuring vibrations parallel to the plate surface.

The dominant frequencies measured perpendicular to the plate surface were 355 Hz and its harmonics (710 and approximately 1060 Hz). These values are similar to the dominant peaks detected without the presence of the second mounting hole in the plate. The 355 and 710 Hz peaks were the only frequencies detected when the accelerometer was mounted in the plane of the plate surface. The intensity of the disturbances was significantly less relative to the magnitude measured perpendicular to the plate surface, and they decreased as the jet velocity increased.

The potential effects of the plate and nozzle vibrations on the sheet were investigated analytically. The wavelength of a disturbance, λ, is related to its frequency, f, and speed, U, that is

$$\lambda = \frac{U}{f}. \tag{18}$$

If the wave speed of the disturbances induced by the plate vibrations is assumed to be equal to the sheet velocity, then the wavelength can be calculated and compared to both the experimentally measured wavelengths and the wavelength of optimum growth predicted by linear theory. This comparison is shown in Fig. 16. For fixed fluid properties, there is a one-to-one correspondence between the sheet velocity and the optimum wavelength. These sheet velocities are shown on the top axis.

Because the range of operating conditions for which disturbance wavelengths were measured was only a fraction of the total range investigated in this study, further assessment of the role of external disturbances on sheet stability was performed analytically. The influence of induced waves relative to the wave of optimum growth can be estimated from the relationship between the wavelength of a sinuous disturbance and its predicted growth rate in an inviscid sheet. The dispersion relation for the sinous mode can be made dimensionless with respect to the wave number of optimum growth , k_{opt}, and its corresponding growth rate, s_{opt}. The resulting dimensionless equation,

$$\frac{k}{k_{opt}} = 1 \pm \sqrt{1 - \left(\frac{s}{s_{opt}}\right)^2} \tag{19}$$

is plotted in Fig. 17. Using the relationship between the wave number of a disturbance and its wavelength ($\lambda = 2\pi/k$), these data are replotted in Fig. 18 as the growth rate versus the wavelength, where both values have been made dimensionless with respect to the optimum

values predicted from linear theory. As can be seen in Fig. 19, the maximum unstable wave number ratio is predicted to be two. Based on linear theory for inviscid sheets, disturbances of higher wave number are expected to be stable. This maximum wave number of two corresponds to a minimum wave length ratio of 0.5, indicating that disturbances with a wavelength of less than half the optimum disturbance wavelength will not grow.

Both the minimum and optimum disturbance wavelengths are functions of the sheet velocity. These wavelengths are calculated for the range of sheet velocities encountered in this study (2-10 m/s) and are plotted in Fig. 19. The line corresponding to the predicted wavelength of a disturbance induced by the 352 Hz vibration discussed earlier is also shown. As can be seen in this plot, below approximately 5 m/s, the 352 Hz disturbance is predicted to be stable and, thus, should have no effect on the breakup of the sheet.

Above 5 m/s, the wavelength of the externally-induced disturbance is unstable. The 352 Hz vibration is predicted to result in a disturbance with a wavelength less than the optimum wavelength for sheet velocities less than about 6 m/s, while above 6 m/s, the induced wavelength will be greater than the optimum wavelength. Based on these results, the following behavior is expected.

The breakup length is expected to decrease with decreasing wavelength and increasing initial amplitude and growth rate. As the sheet velocity increases, the wavelength of the optimum disturbance decreases while its growth rate increases, and the sheet is expected to reach a given level of thinning closer to the plate edge. This effect is enhanced by the external driving of a disturbance near the optimum wavelength, corresponding to an increase in the initial disturbance amplitude. When the sheet velocity is approximately 6 m/s, the external disturbance corresponds to the wavelength of optimum growth, and the greatest decrease in the breakup distance is expected. As the sheet velocity is further increased, the optimum disturbance

wavelength is still predicted to decrease while its growth rate increases, thus suggesting that the breakup length should continue to decrease. This would be true for a system free from external disturbances; however, because the 352 Hz disturbance is no longer the optimally growing disturbance, the initial amplitude of this disturbance is no longer enhanced, and the breakup length is expected to increase.

DISCUSSION

A radially thinning free sheet is formed by a splash plate nozzle. This sheet thins due to both the radial expansion of the sheet and the growth of sinuous waves resulting from the hydrodynamic instability of disturbances. When the sheet thickness is sufficiently reduced, local rupture occurs. The resulting holes grow rapidly, and the rims surrounding them interact to form clumps and strands of liquid. These clumps and strands break up into the observed drop size distribution. Several steps in this processes are examined in greater detail, as summarized below.

The predicted effects of the jet velocity and orifice diameter on the sheet thickness correspond qualitatively to their observed effects on the number of perforations formed. It was concluded that the combination of the radial and wave thinning reduces the sheet thickness to a critical value, at which point rupture occurs.

Images obtained with a high-speed 16 mm camera were used to measure the growth rates of perforations in the sheet. These growth rates were used to calculate the thickness of the sheet. These calculated thicknesses were significantly less than the thickness predicted in the absence of waves. This provides support for a wave-thinning induced sheet rupture mechanism; however, the measured thickness was still one to two orders of magnitude larger than the maximum sheet thickness predicted for spontaneous rupture; thus, other mechanisms of rupture may be important. The formation of perforations has been attributed to a number of causes.

Unwettable particles in the fluid are expected to cause rupture when the thickness of the sheet is reduced to the characteristic dimension of the particles. Based on the perforation growth rate data, holes are first formed when the sheet thickness is about 5-20 microns. As no attempt was made to protect the test fluid from airborne dust, particles in this size range may have been present in the system and could be the causative agent of rupture.

In addition to the presence of airborne contaminants, air bubbles may also be present. The test fluid was recirculated throughout each run and may have entrained micron-sized air bubbles. Larger bubbles were detected in several high-speed 16 mm films, but the flow loop and operating procedures were modified to eliminate them from other runs. In subsequent films, the number of visible air bubbles was significantly reduced, but the resolution of the images was not great enough to detect bubbles smaller than approximately 100 microns (0.1 mm).

While air bubbles are not unwettable particles, their presence would result in sheet rupture. When the wave-thinned sheet thickness is reduced to the characteristic dimension of the bubble, the minimum local thickness will equal the thickness of the bubble film. This thickness will be significantly less than that of the surrounding liquid sheet and may be below the critical thickness for spontaneous rupture.

The process by which an entrained air bubble may result in rupture is sketched in Fig. 20. When the sheet thickness is much greater than the bubble dimension, the presence of entrained air has a minimal effect on the sheet (see Fig. 20a). As radial expansion and waves thin the sheet, the thickness of the sheet will approach the characteristic dimension of the bubble (see Fig. 20b). When the sheet thickness is less than or equal to the bubble diameter, a local thin spot will occur, where the thinnest dimension is equal to the bubble film thickness (see Fig. 20c). If this thickness is less than the critical film thickness for spontaneous rupture, the bubble film will burst creating a hole in the sheet with a radius equal to the radius of the bubble (see Fig. 20d). Based on Taylor and Michael's[21] analysis, this hole will grow if the bubble radius is greater than the sheet thickness; however, this result was based on a balance of surface tension forces acting on a hole in a sheet at equilibrium. For the case of a hole formed from a bursting bubble, there are additional destabilizing effects associated with the inertia of the rupturing bubble. Thus, the local sheet thickness may be considered an upper bound for the minimum bubble radius needed to cause a growing perforation.

A sample of the glycerol/water solution is examined under an optical microscope at 200X magnification. Numerous air bubbles, ranging in size from approximately 5-100 microns, are observed, as shown in Fig. 21. Most of the bubbles shown are less than 20 microns in diameter, but a 90 μm bubble can also be seen. Although solid particles are also observed, the number of air bubbles seen is far greater.

The air bubbles observed are known to be entrained in the fluid during the spraying and recirculation processes.

The time required for an air bubble to rise out of a glycerol/water solution is calculated based on its terminal velocity. Bubbles in the size range of 1 to 20 microns are found to be in the Stoke's flow range ($Re << 1$). For a glycerol/water solution with a viscosity of 0.05 kg/m·s, bubbles 1 μm in diameter would require about 2100 hours to rise 10 centimeters, while 20 μm bubbles would rise the same distance in about 6 hours. (Because the bottom of the tank is sloped, the depth of fluid varies from 8 to 14 cm.) The time required for a 1 μm and a 20 μm bubble to rise 10 centimeters through a solution with a viscosity of 0.1 kg/m·s would be 4200 hours and 11 hours, respectively. Based on these results, it is concluded that small air bubbles (less than 20 μm) were present in the spray experiments performed in this study and are believed to be the dominant cause of liquid sheet rupture.

The impingement of drops on the sheet has also been cited as a cause of rupture. Although no drops forming at the nozzle or deflecting off the tank walls were observed striking the sheet, a fraction of the drops formed in the region of breakup appeared to have an upstream component of velocity. These drops might strike and puncture the sheet.

The wave-thinning analysis performed in this study was based on the growth of a single wave; however, as shown in the images of the rims formed by splitting the sheet, the wave shapes did not correspond to a single sine wave. This result could be used to infer that the sheet

is perturbed by two or more interacting waves. This interaction may lead to sheet thickness variations in addition to the radial and single-wave thinning mechanisms.

At least two disturbance wavelengths are expected based on the vibration analysis and wavelength measurement results. The measured wavelength appears to follow the trends predicted by linear theory, while the FFT spectra suggest the presence of an additional wave with a frequency of about 352 Hz. The results of the perforation count experiments demonstrated that, when this wavelength of the disturbance resulting from this vibration was near the wavelength of optimum growth, the breakup length was reduced. Even when the vibration-induced wavelength is significantly different from the optimum wavelength, the two waves will interact to enhance the rate of wave thinning and, thus, reduce the breakup length.

In addition to the observed sinuous waves, dilational waves are also expected to be present. Although dilational waves are found to thin the sheet more slowly than sinuous waves, these dilational waves are still expected to contribute to the total rate of thinning.

Certain features are common to all of these mechanisms of rupture. First, each process is random, that is the location of the particle, bubble, or impinging drop causing each rupture cannot be predicted, and the initial amplitude and phase lag of vibration-induced waves relative to the aerodynamically-induced waves is not known. Also, it is reasonable to expect that all mechanisms could be active in real spray systems and do not represent a feature particular to this study. Finally, each mechanism requires the prior thinning of the sheet by other processes. In the case of the airborne contaminants and air bubbles, this thickness is related to the dimension of the particles, while for impinging drops, it will be a function of the size and momentum of each drop. In our experiments, the evidence indicates that although all of the mechanisms outlined above may contribute to the sheet rupture, the presence of very small invisible air bubbles is the dominant mechanism.

NOMENCLATURE

d_0	nozzle orifice diameter
e	growth rate of a perforation
h	sheet half-thickness (2h = full thickness of the sheet)
K_N	function of the nozzle geometry and the flow characteristics of the sheet.
k_{opt}	number of optimum growth
k*	dimensionless wave number, is defined as the ratio of the wave number to the wave number of optimum growth in an inviscid sheet
Np_{area}	area corrected number of perforations at downstream position per centimeter of radial span
Np_{obs}	number of perforations observed at downstream position
Re_{jet}	the jet Reynolds number
R_p	the radius of a perforation
S	radial span of the imaging area
s_{opt}	growth rate
U_0	jet velocity
$U_{s,avg}$	average sheet velocity
W	lateral width of the imaging area
We_{jet}	the jet Weber number
x	radial position downstream from the point of jet impact

x_p downstream location of the plate edge

x_t downstream location where the boundary layer over the plate becomes fully developed.

ρ_{liq} liquid density

λ wavelength of a disturbance

LITERATURE CITED

1. Masters, K. Spray Drying Handbook. George Goodwin Limited, London, 1985

2. Lefebvre, A.H. Atomization and Sprays. Combustion: An International Series, N. Chigier ed., Hemisphere Publishing Corp., 1989.

3. Lefebvre, A.H. Fuel Atomization, Droplet Evaporation, and Spray Combustion. Chapter Nine in: Fossil Fuel Combustion. Ed. Bartok, W.; Sarofim, A.F., John Wiley and Sons Inc., 1991.

4. Taylor, G.I. Oblique Impact of a Jet on a Plane Surface. Phil. Trans. Roy. Soc. London A(260):96-100(1966).

5. Taylor, G.I. Formation of Thin Flat Sheets of Water. Proc. Roy. Soc. London A(259):1-17(November 1960).

6. Taylor, G.I. The Dynamics of Thin Sheets of Fluid I. Water Bells. Proc. Roy. Soc. London A(253):289-95(December 1959).

7. Taylor, G.I. The Dynamics of Thin Sheets of Fluid III. Disintegration of Fluid Sheets. Proc. Roy. Soc. London A(253):313-21(December 1959).

8. Watson, E.J. The Radial Spread of a Liquid Jet Over a Horizontal Plane. J. Fluid Mech., 20(Part 3):481-99(1964).

9. Huang, J.C.P. The Breakup of Axisymmetric Liquid Sheets. J. Fluid Mech., 43(2):305-19(1970).

10. Dombrowski, N.; Fraser, R.P. A Photographic Investigation into the Disintegration of Liquid Sheets. Phil. Trans. Roy. Soc. London, 247A:101-30(September 1954).

11. Fraser, R.P.; Eisenklam, P.; Dombrowski, N.; Hasson, D. Drop Formation from Rapidly Moving Liquid Sheets. A.I.Ch.E. J., 8(5):672-80(November 1962).

12. Xianguo Li; Tankin, R.S. On the Temporal Instability of a Two-Dimensional Viscous Liquid Sheets. J. Fluid Mech., 226:425-43(1991).

13. Dombrowski, N.; Johns, W.R. The Aerodynamic Instability and Disintegration of Viscous Liquid Sheets. Chem. Eng. Sci., 18:203-13(1963).

14. Weihs, D. Stability of Thin, Radially Moving Liquid Sheets. J. Fluid Mech., 87(Part 2):289-98(1978).

15. Hagerty, W.W.; Shea, J.F. A Study of the Stability of Plane Fluid Sheets. J. Appl. Mech., 22:509-514(December 1955).

16. Clark, C.J.; Dombrowski, N. The Dynamics of the Rim of a Fan Spray Sheet. Chem. Eng. Sci., 26:1949-52(1971).

17. Sheludko, A. Thin Liquid Films. Advan. Colloid Interface Sci., Elsevier Publishing Company, Amsterdam, 1:391-464(1967).

18. Patzer, J.F.; Homsey, G.M. Hydrodynamic Stability of Thin Spherically Concentric Fluid Shells. J. Colloid and Interface Science, 51(3):499-508(June 1975).

19. Pandit, A.B.; Davidson, J.F. Hydrodynamics of the Rupture of Thin Liquid Films. J. Fluid Mech., 212:11-24(1990).

20. Taylor, G.I.; Michael, D.H. On Making Holes in a Sheet of Fluid. J. Fluid Mech., 58(part4):625-39(1973).

21. Spielbauer, T., "Droplet Formation from a Radially Expanding Liquid Sheet," Ph.D. Thesis, Institute of Paper Science and Technology, Atlanta, GA., 1993..

22. Asare, H.R.; Takahashi, R.K.; Hoffman, M.A. Liquid Sheet Jet Experiments: Comparison with Linear Theory. J. Fluids Engineering, 103:595-604(December 1981).

23. Spielbauer, T. and Aidun, C.K., Mechanism of Liquid Sheet Breakup and the Resulting Drop Size Distribution. Tappi J., Parts I and II, 75 (2 and 3): 136, 1992.

24. Spielbauer, T.M., and Aidun, C.K., The Wave Thinning and Breakup of Liquid Sheets, Submittted for publication, 1993.

LIST OF FIGURE CAPTIONS

Figure 1. A splash plate nozzle.

Figure 2. Sketch of the experimental spray apparatus.

Figure 3. Sketch of the nozzle geometry.

Figure 4. Formation, growth, and interaction of perforation.

Figure 5. Perforation growth and sheet folding.

Figure 6. Liquid sheet in the region of breakup.

Figure 7. (a) Growing sinuous wave disturbance and (b) breakup of a radially thinning sheet.

Figure 8. Representative imaging area for the perforation count experiments.

Figure 9. Reported perforation count versus downstream location: NF-6000 nozzle.

Figure 10. Reported perforation count versus downstream location: NF-8000 nozzle.

Figure 11. Reported perforation count versus downstream location: NF-10000 nozzle.

Figure 12. Predicted downstream sheet thickness.

Figure 13. Number of perforations as a function of downstream sheet thickness.

Figure 14. Comparison of measured and predicted disturbance wavelength.

Figure 15. FFT spectra of the vibrations at the splash plate (U_0=21.9 m/s).

Figure 16. Comparison of the vibration-induced disturbance wavelengths.

Figure 17. Dimensionless growth versus dimensionless wave number.

Figure 18. Dimensionless growth rate versus dimensionless wavelength.

Figure 19. Optimum and minimum wavelength as a function of the sheet velocity based on linear, inviscid theory.

Figure 20. Perforation initiation by an air bubble rupture mechanism.

Figure 21. Typical images of entrained air bubbles (at 200X magnification).

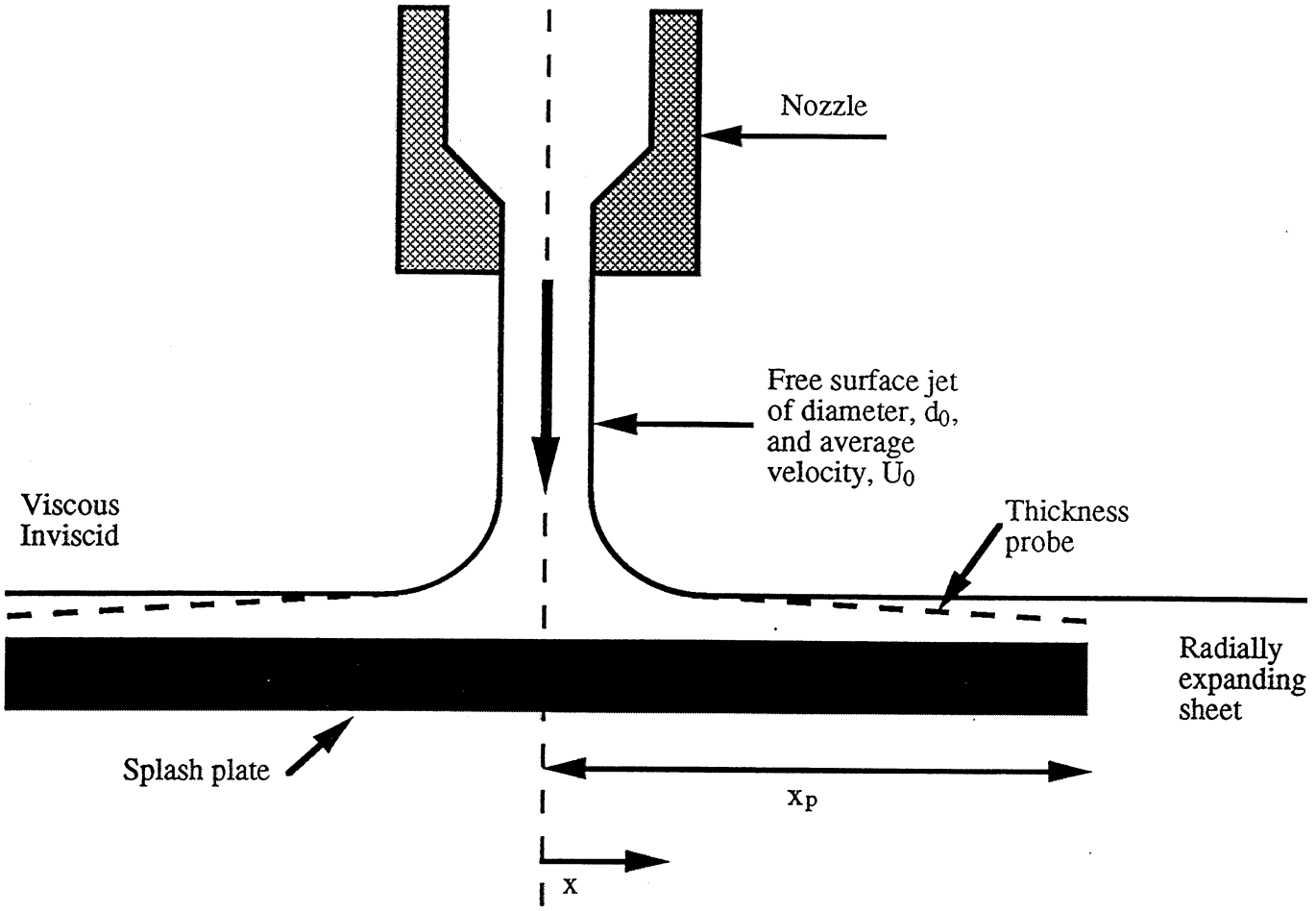

Figure 1. A splash plate nozzle.

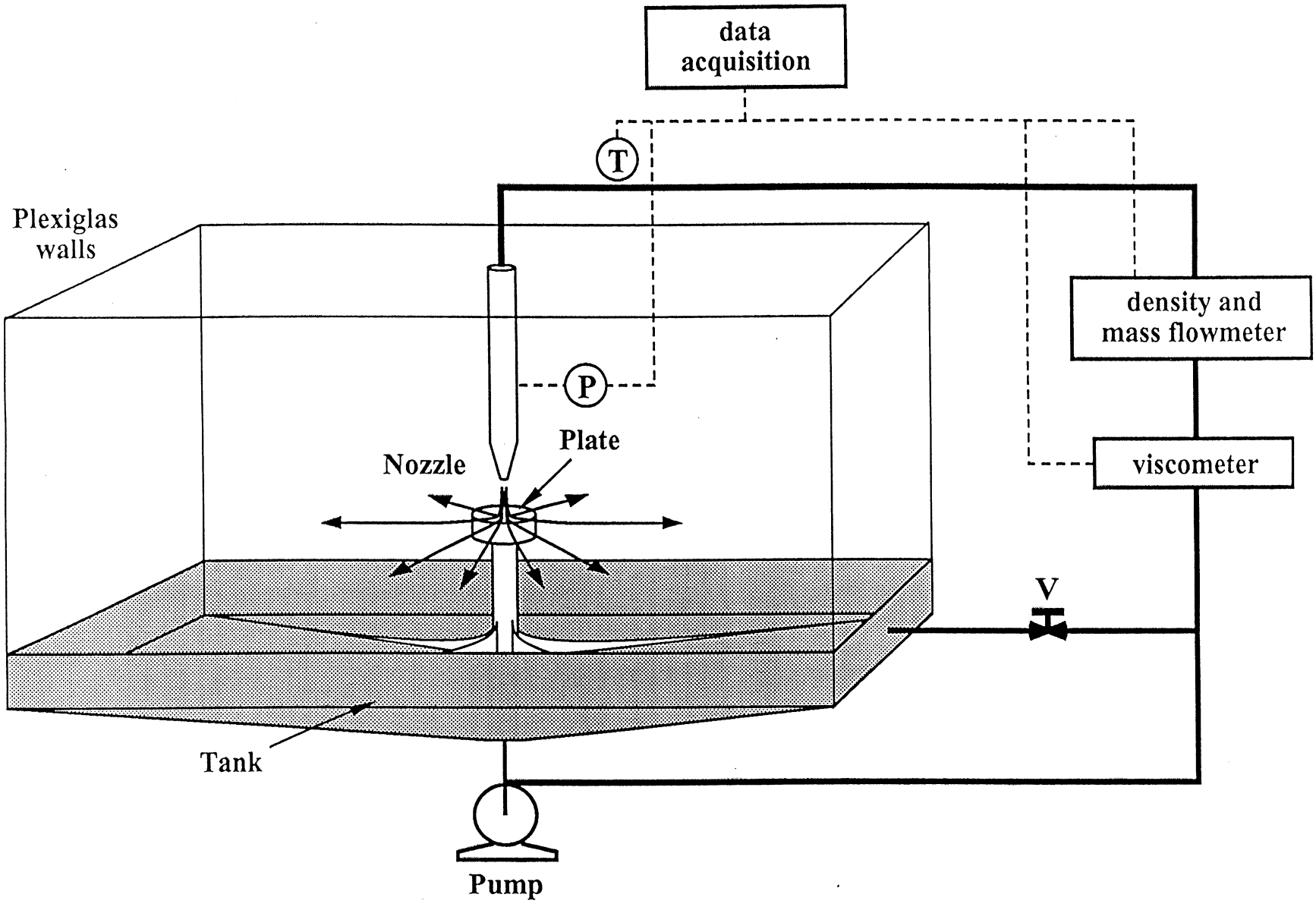

P = flush mounted pressure transducer
T = type-J thermocouple
V = flow control

Figure 2. Sketch of the experimental spray apparatus.

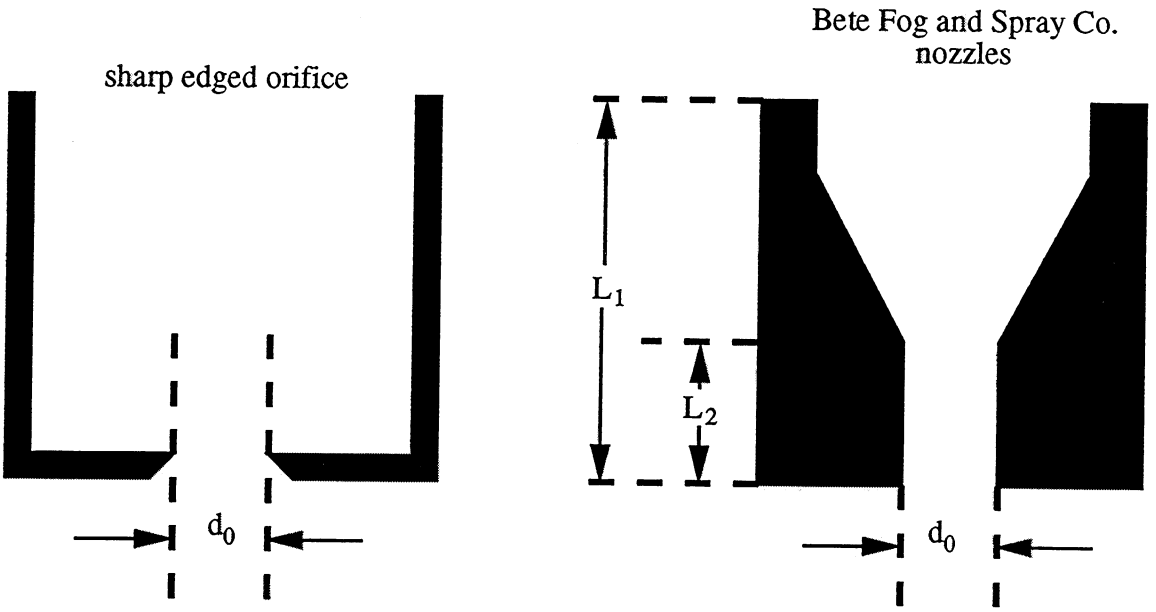

Figure 3. Sketch of the nozzle geometries.

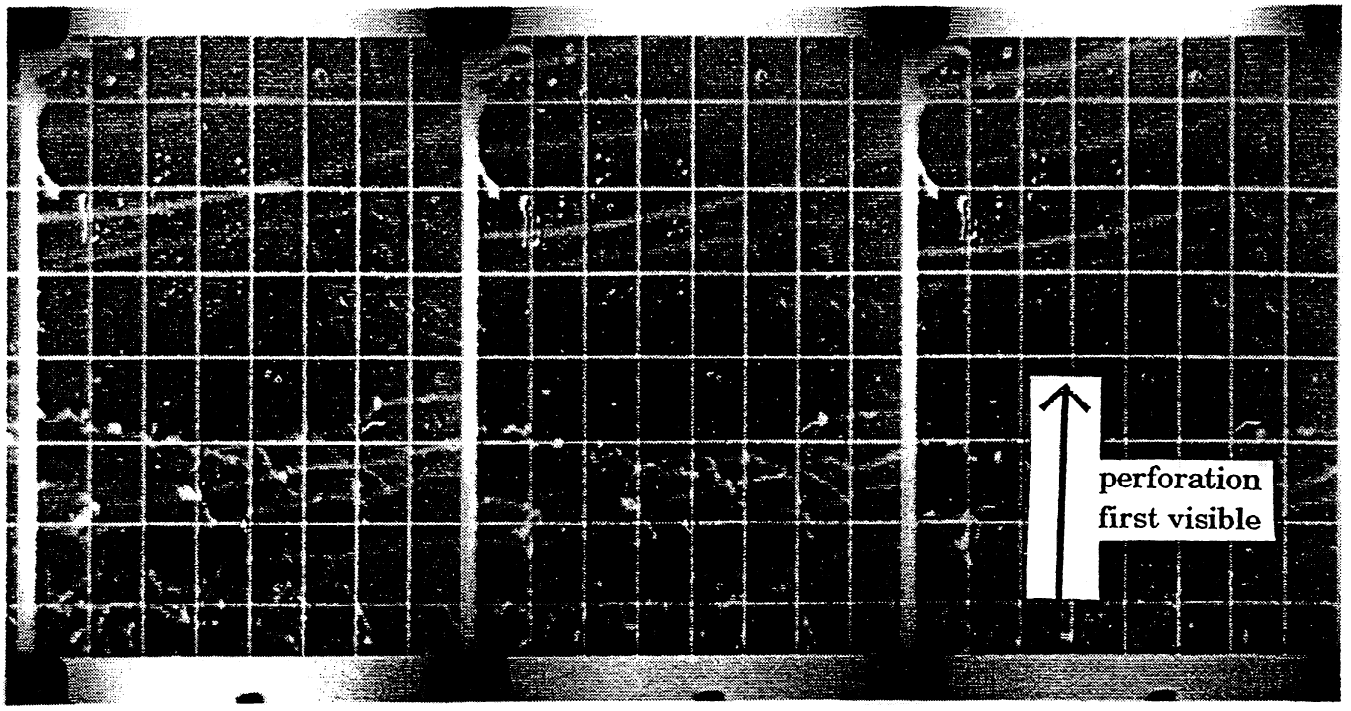

(a) (b) (c)

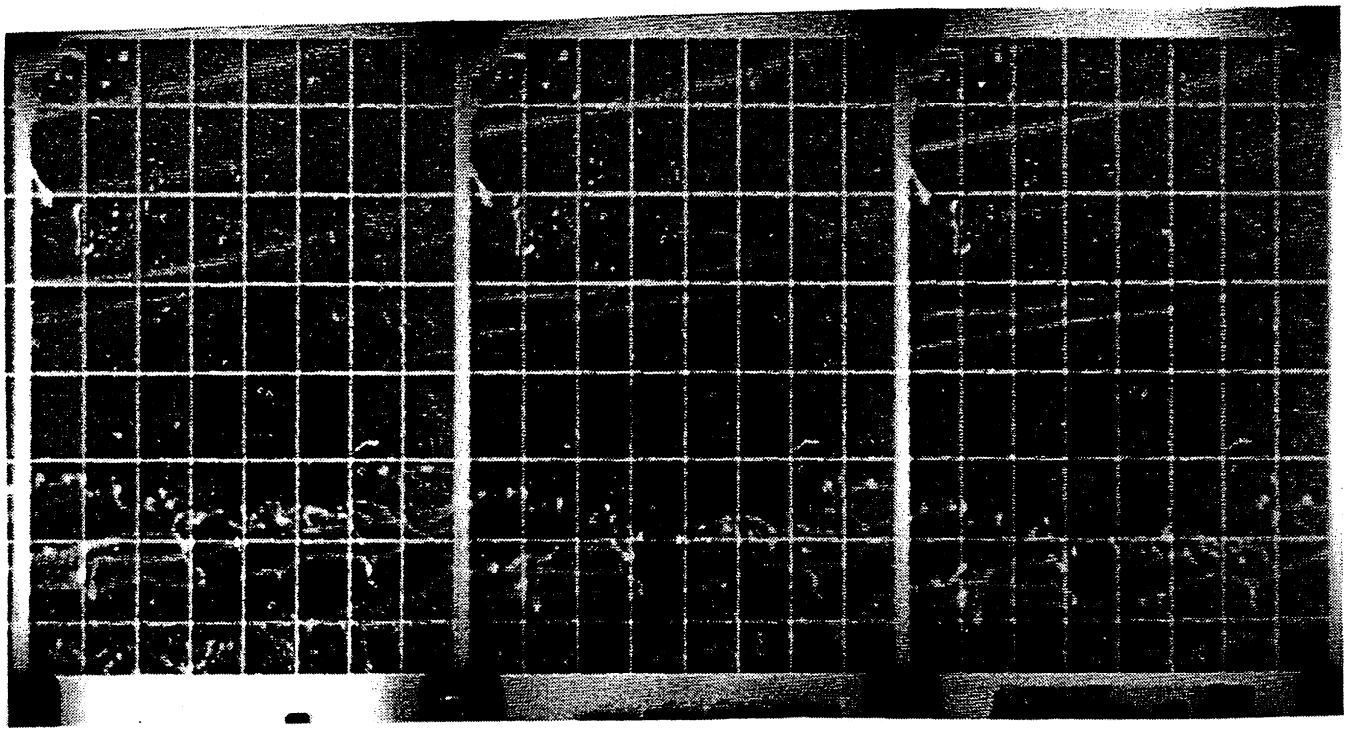

(d) (e) (f)

FIG. 4

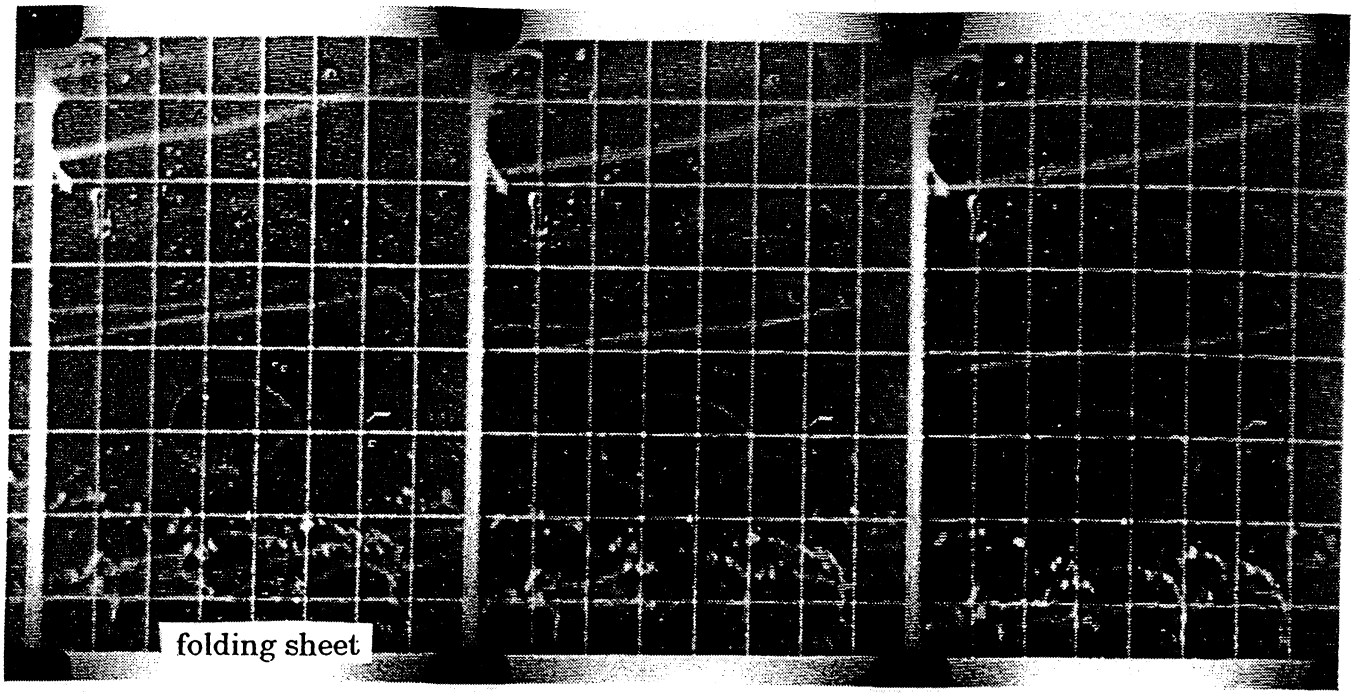

(g) (h) (i)

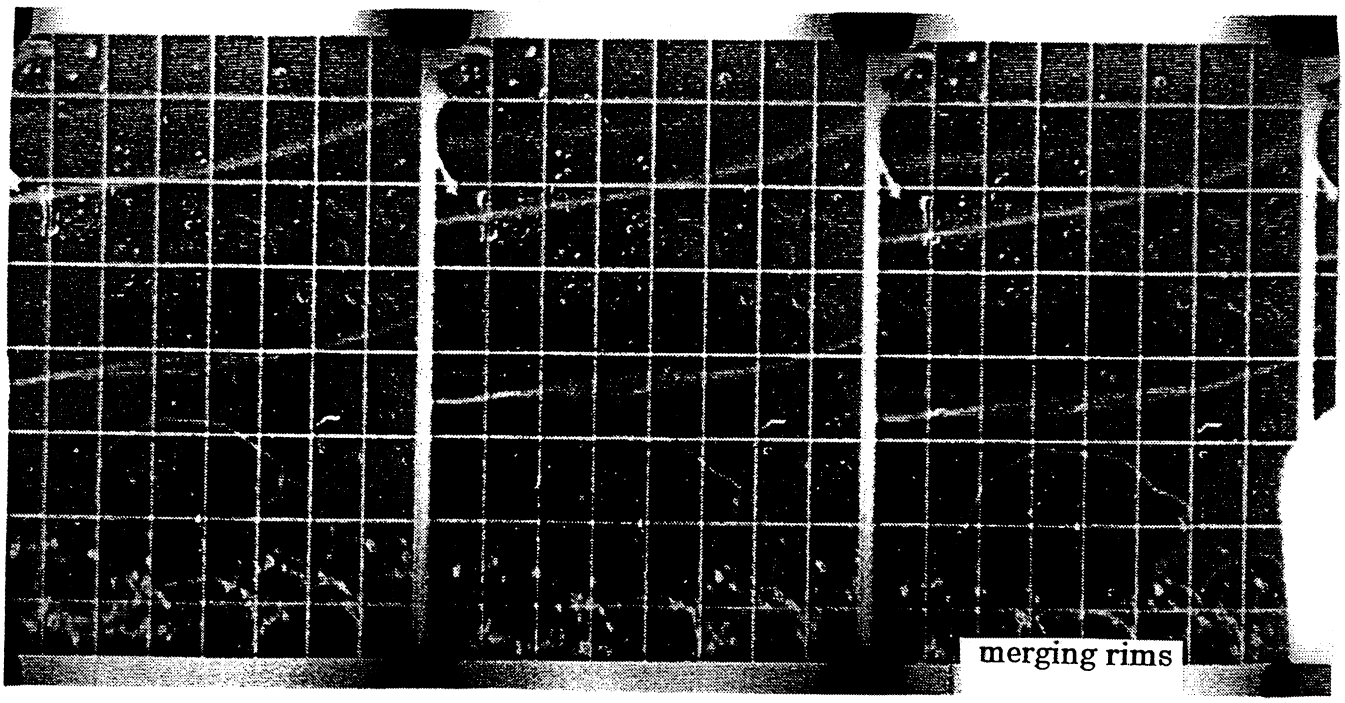

(j) (k) (l)

FIG. 4 (Cont'd)

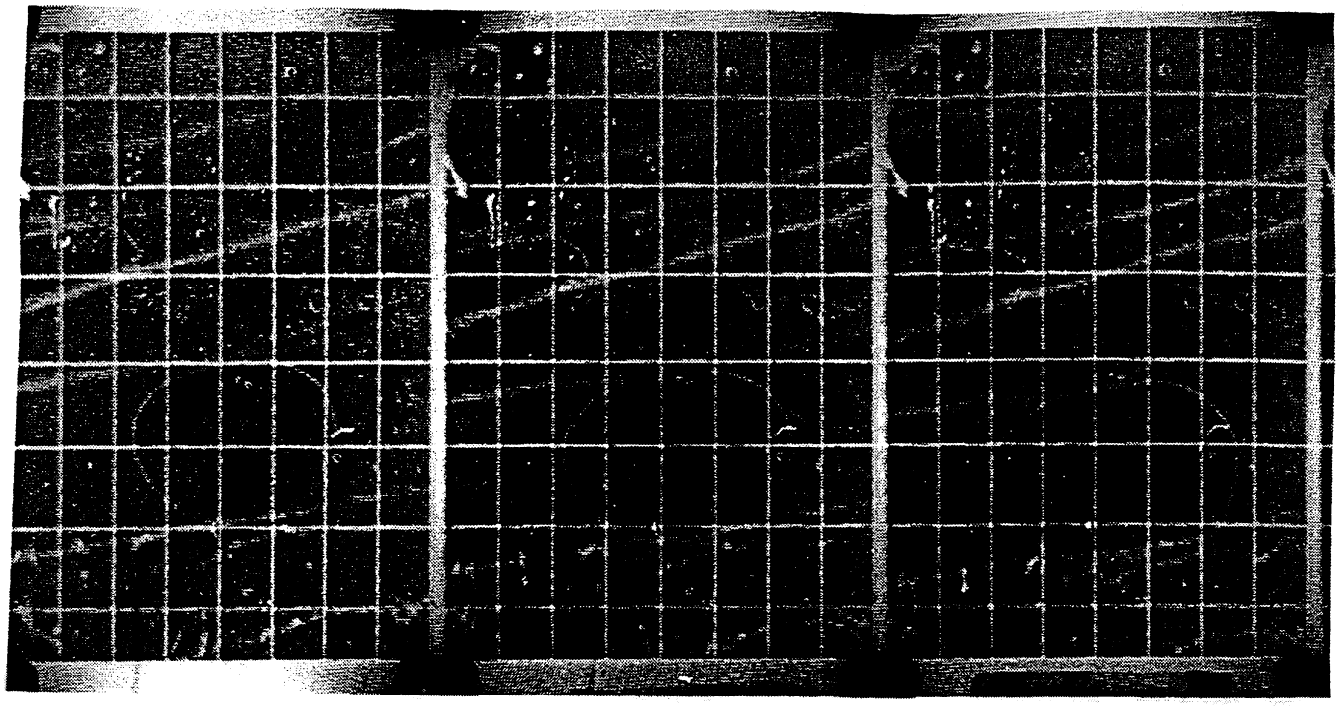

(a) (b) (c)

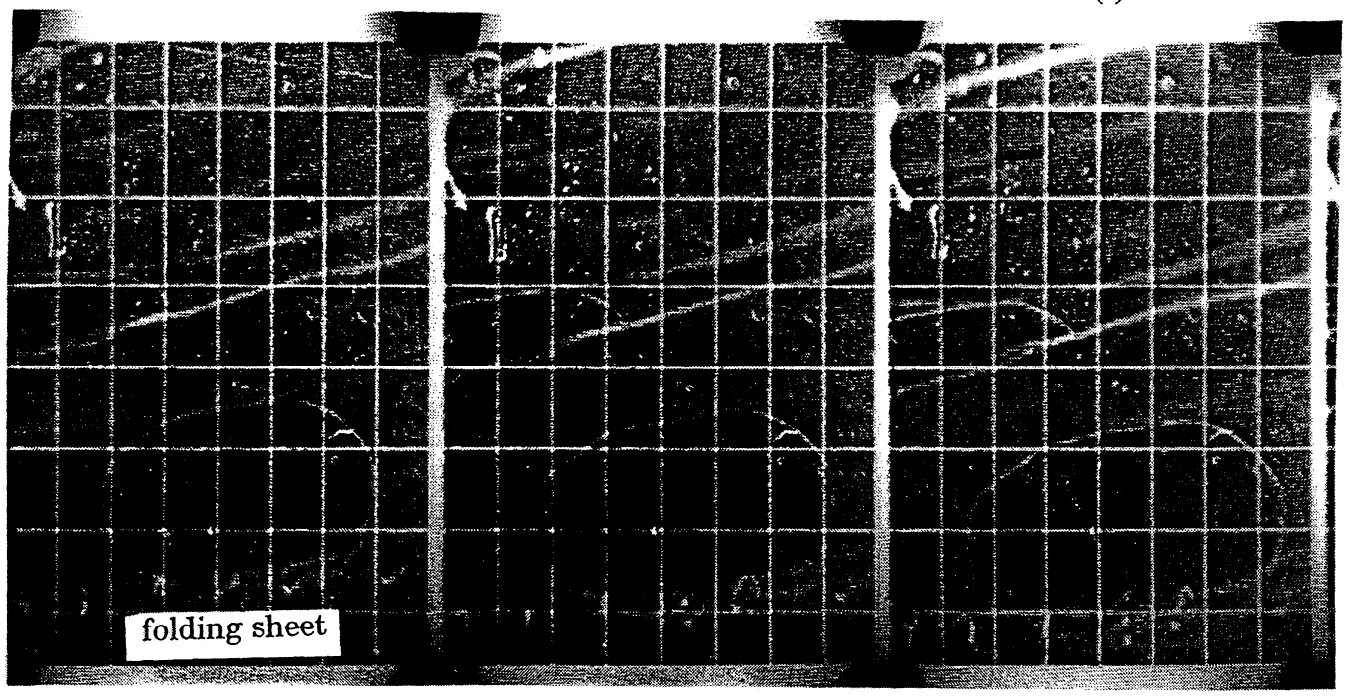

(d) (e) (f)

FIG 5

FIG. 6

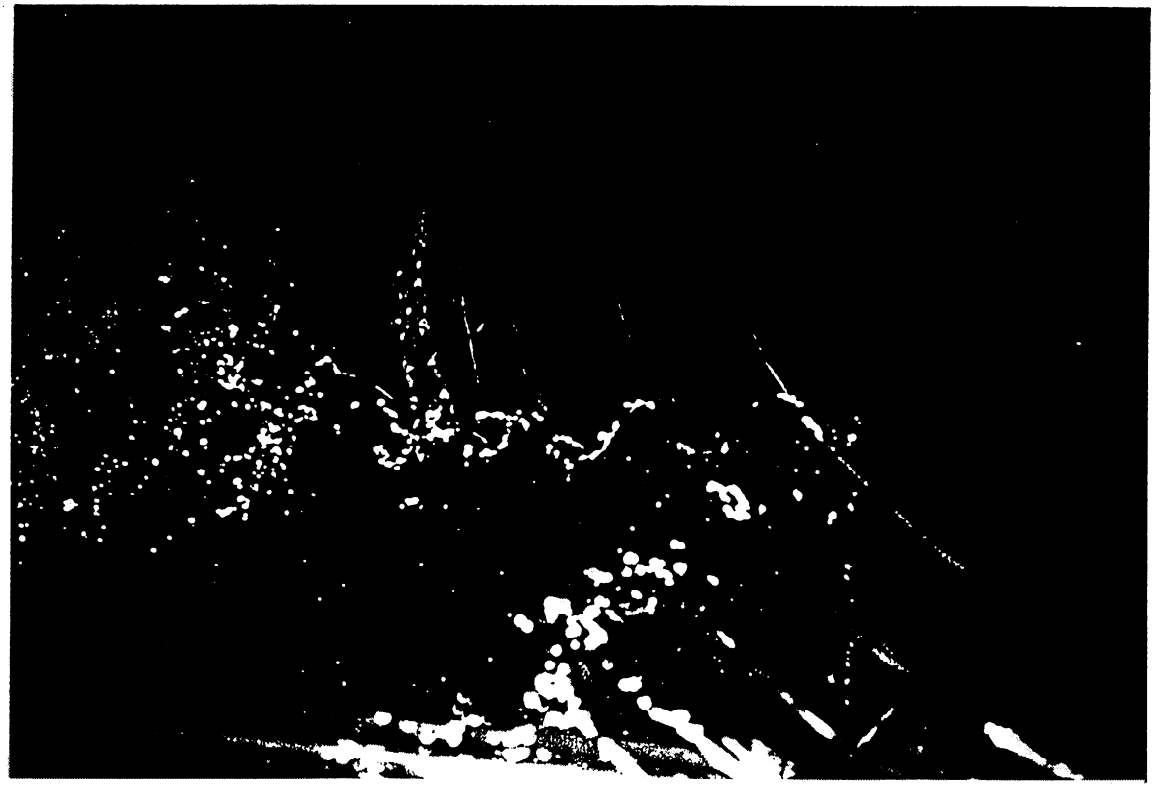

FIG. 7a

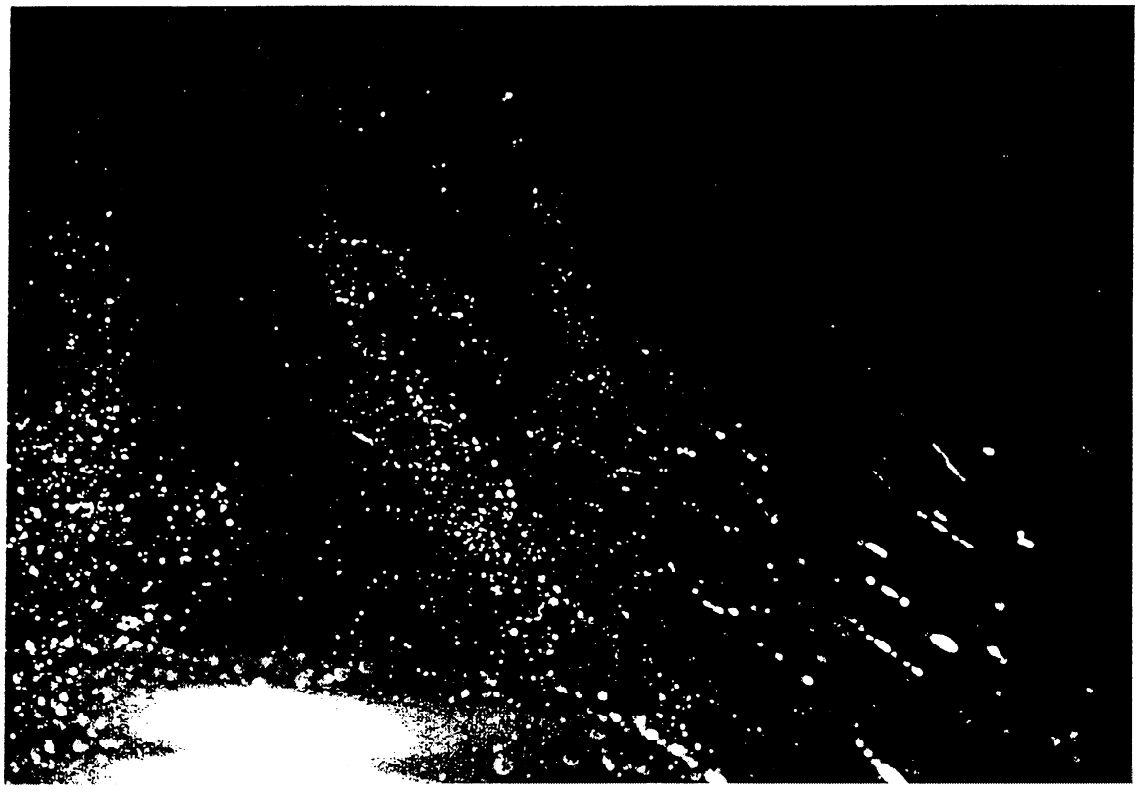

FIG. 7b

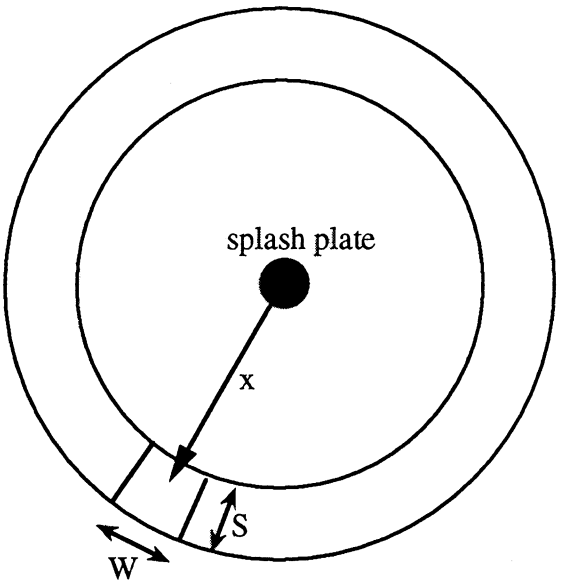

Figure 8. Representative imaging area for the perforation count experiments.

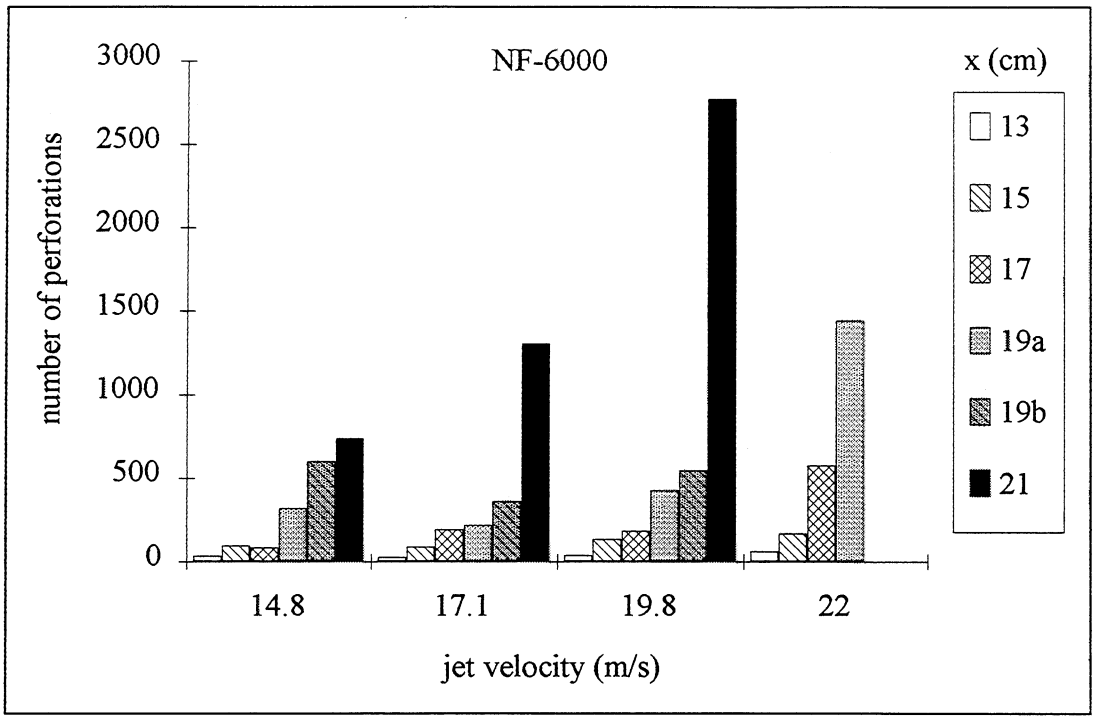

Figure 9. Reported perforation count versus downstream location: NF-6000 nozzle.

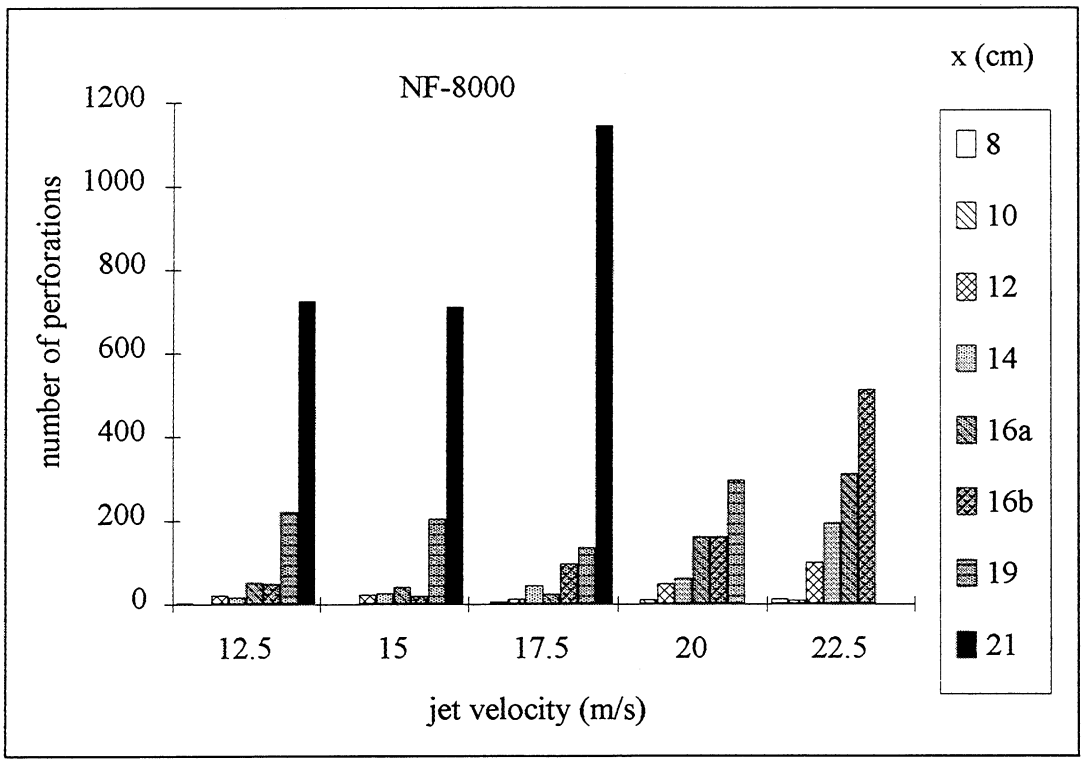

Figure 10. Reported perforation count versus downstream location: NF-8000 nozzle.

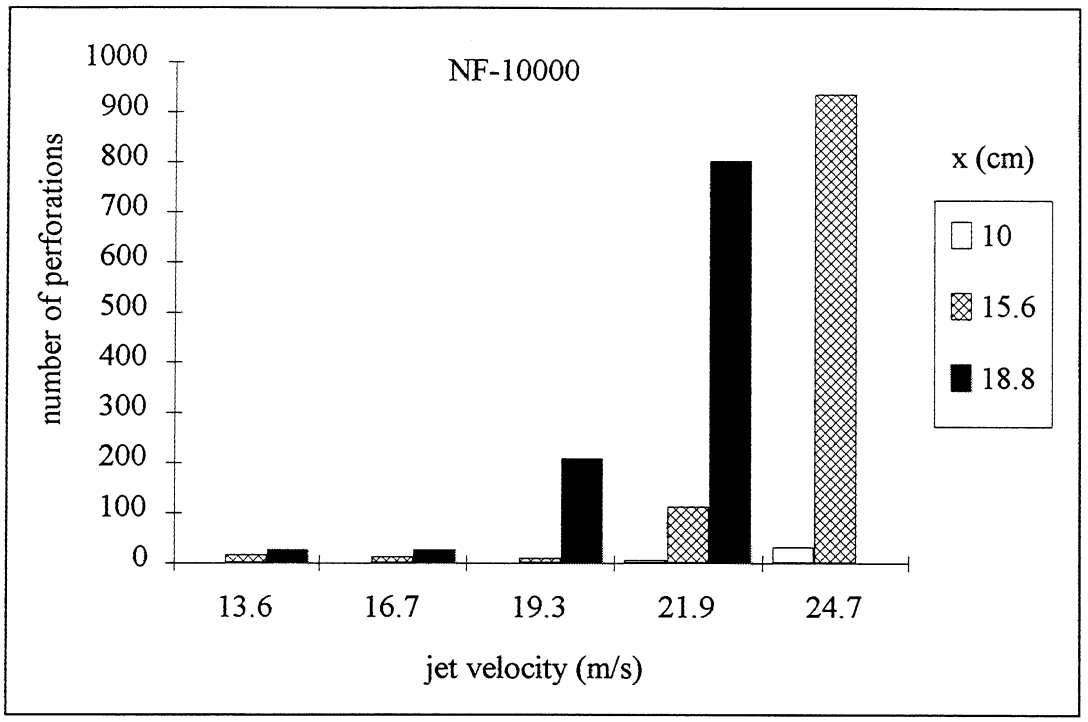

Figure 11. Reported perforation count versus downstream location: NF-10000 nozzle.

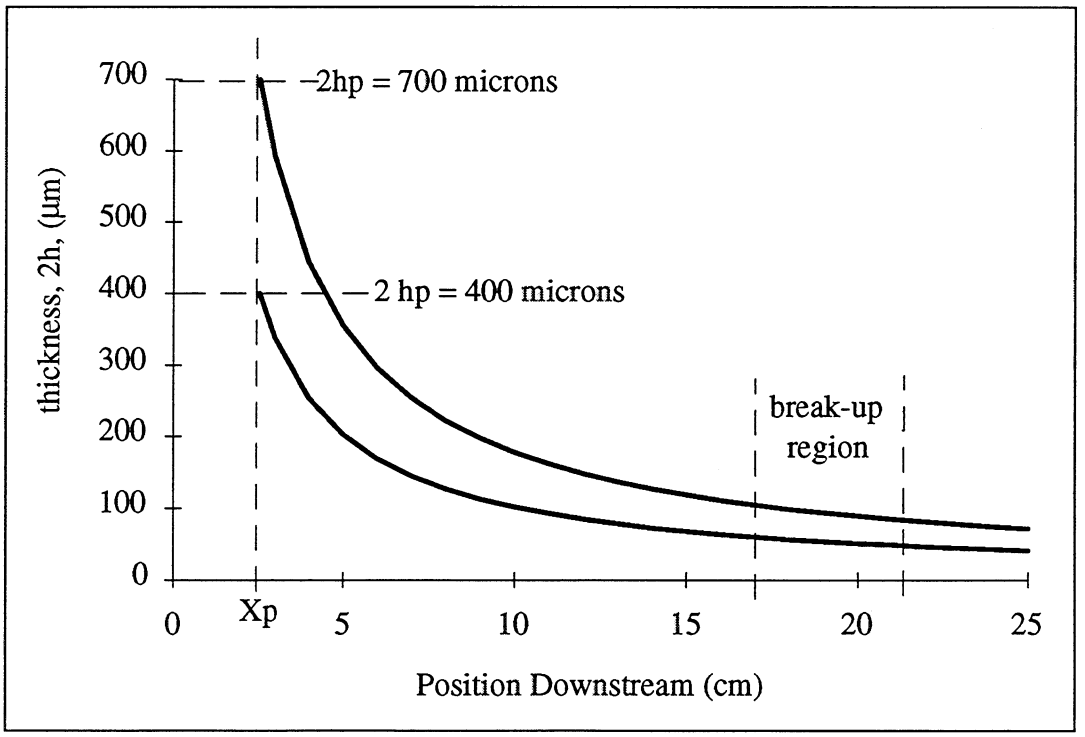

Figure 12. Predicted downstream sheet thickness.

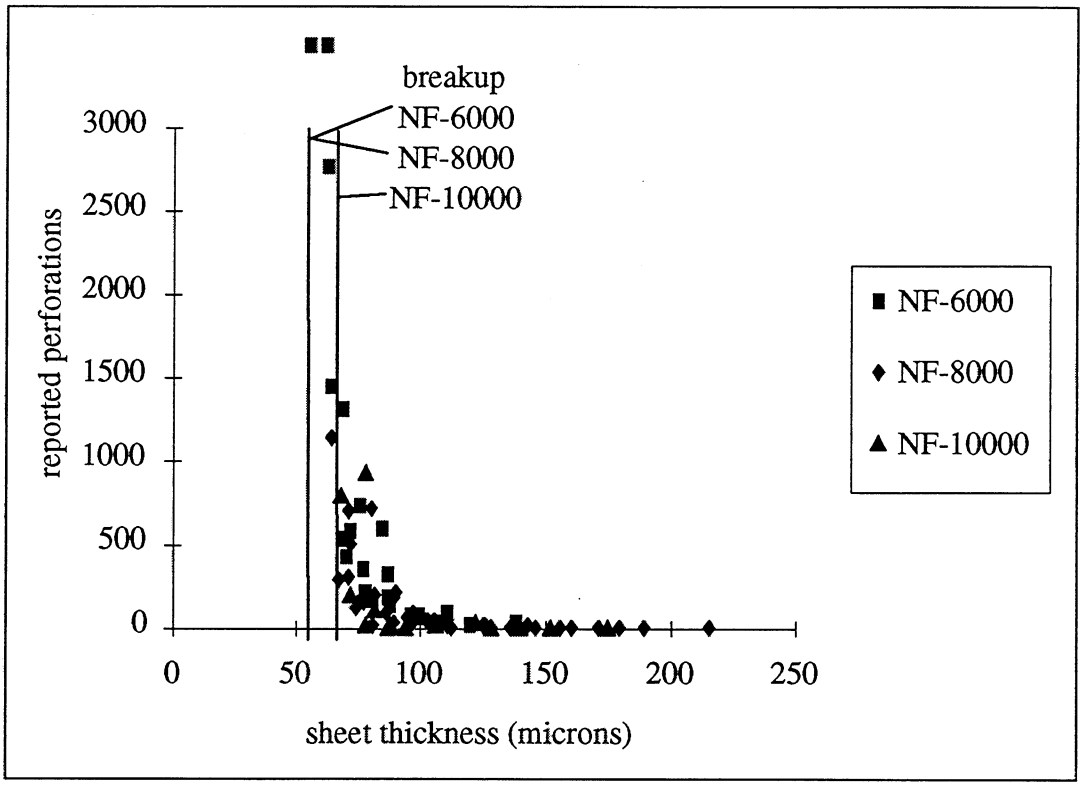

Figure 13. Number of perforations as a function of downstream sheet thickness.

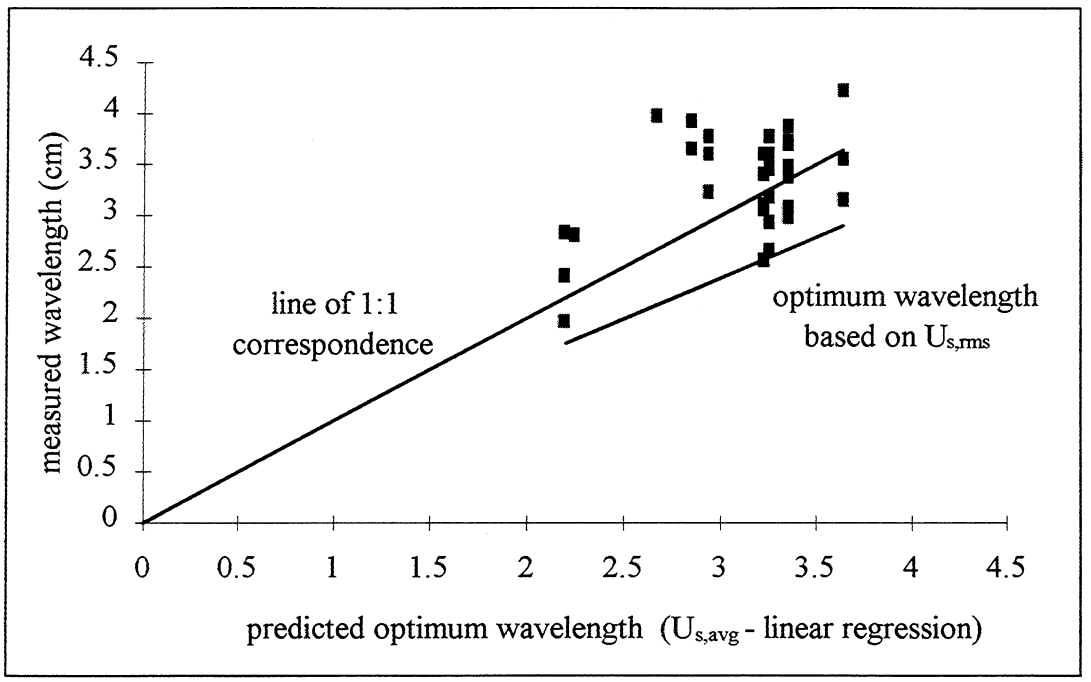

Figure 14. Comparison of measured and predicted disturbance wavelengths.

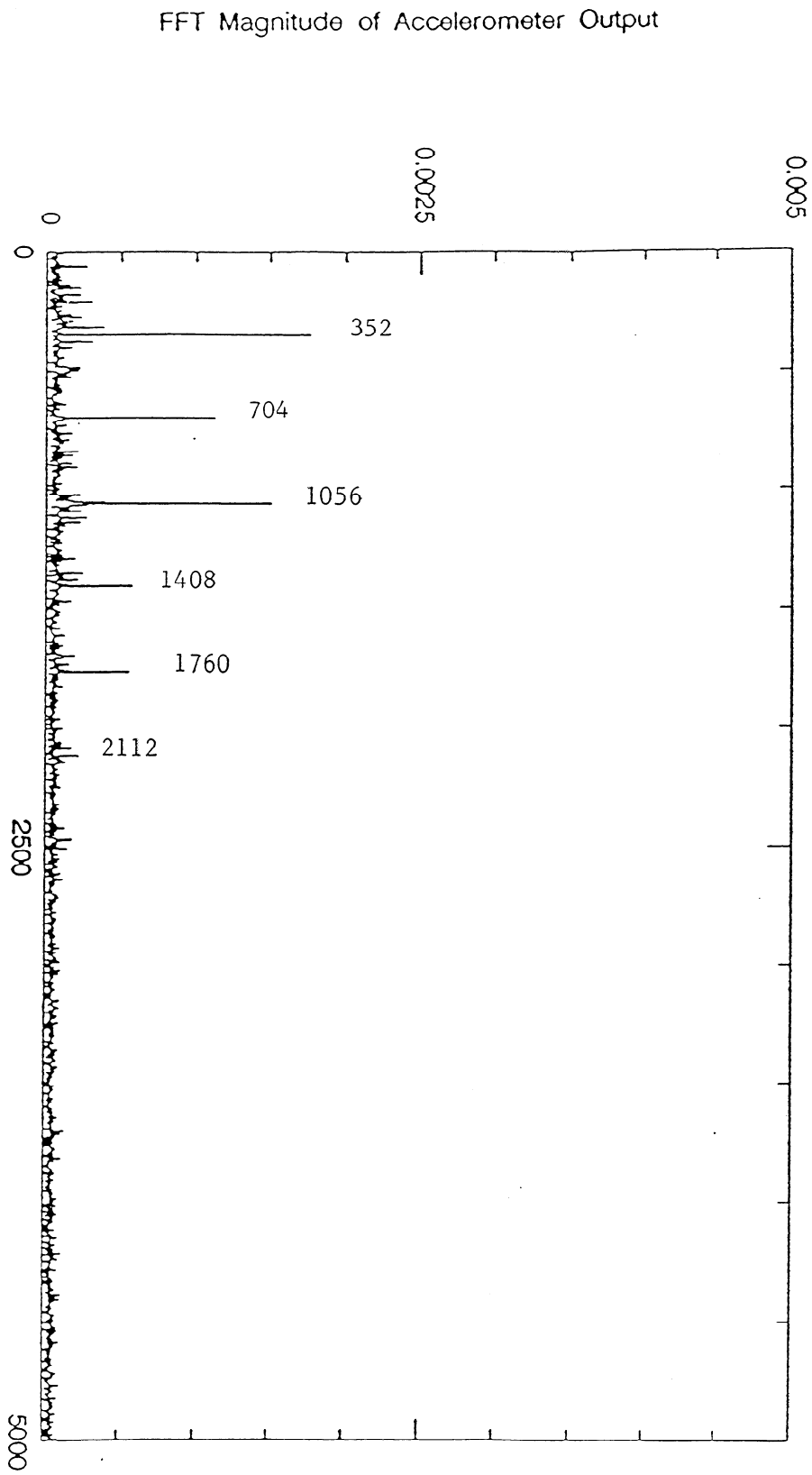

Figure 15. FFT spectra of the vibrations at the splash plate (U_0 = 21.9 m/s).

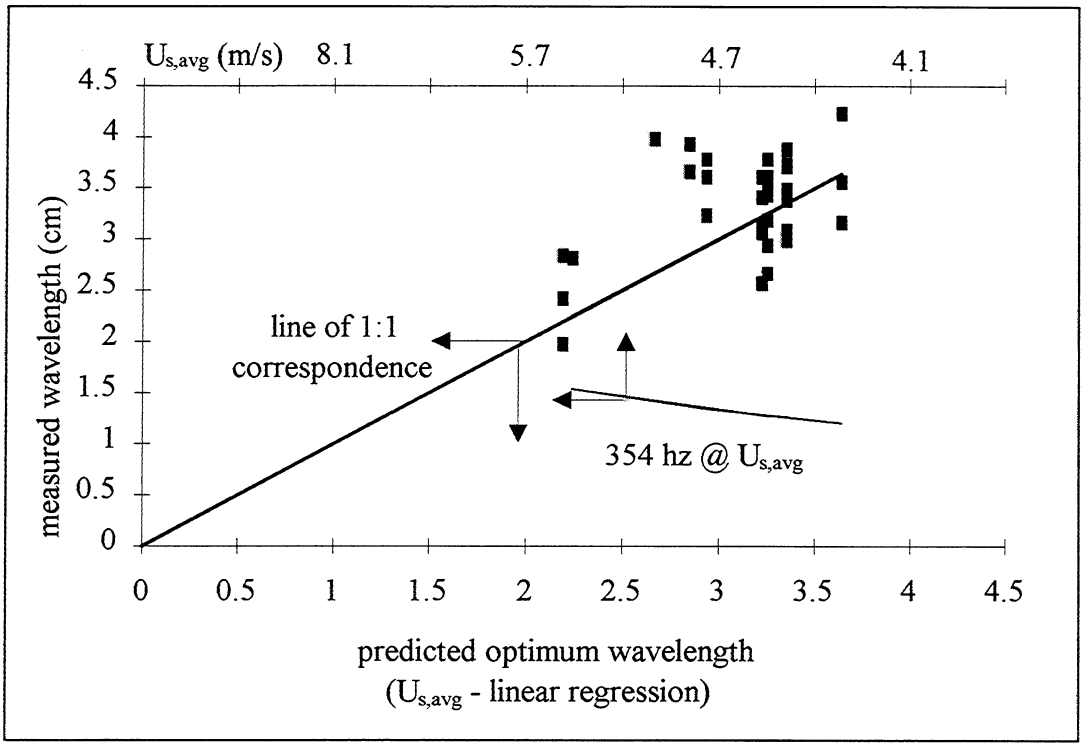

Figure 16. Comparison of the vibration-induced disturbance wavelengths.

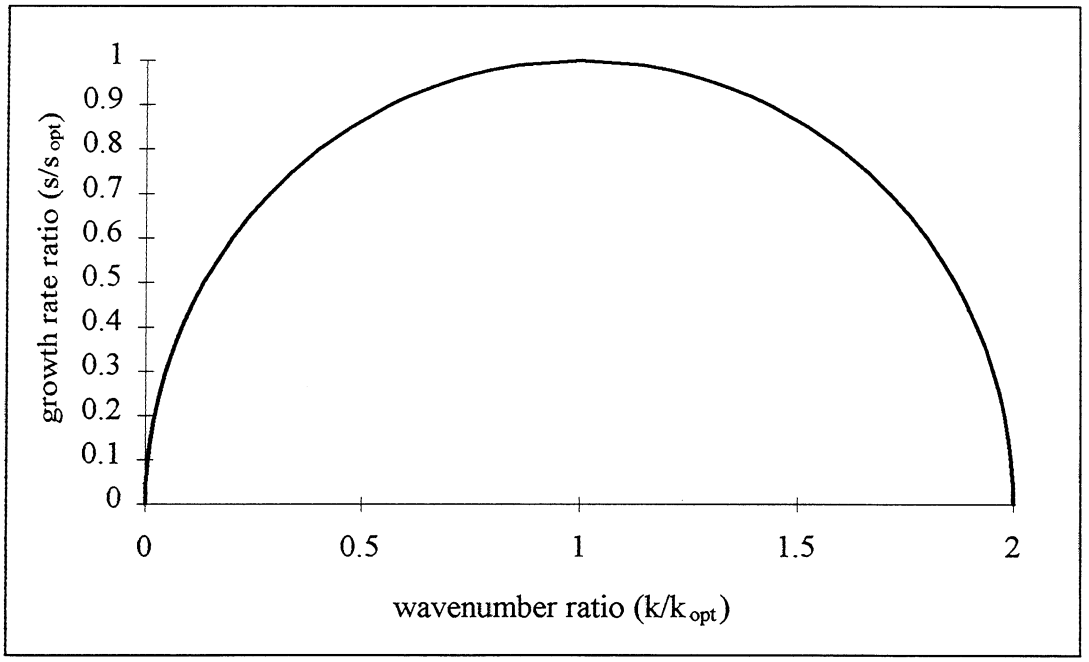

Figure 17. Dimensionless growth rate versus dimensionless wave number.

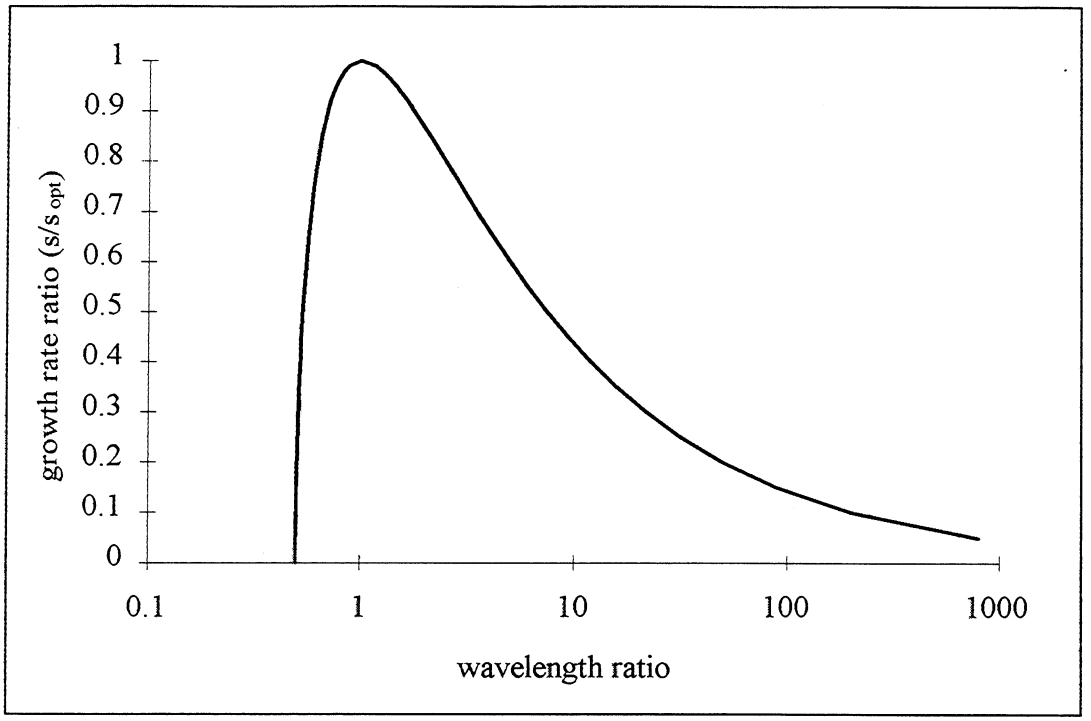

Figure 18. Dimensionless growth rate versus dimensionless wavelength.

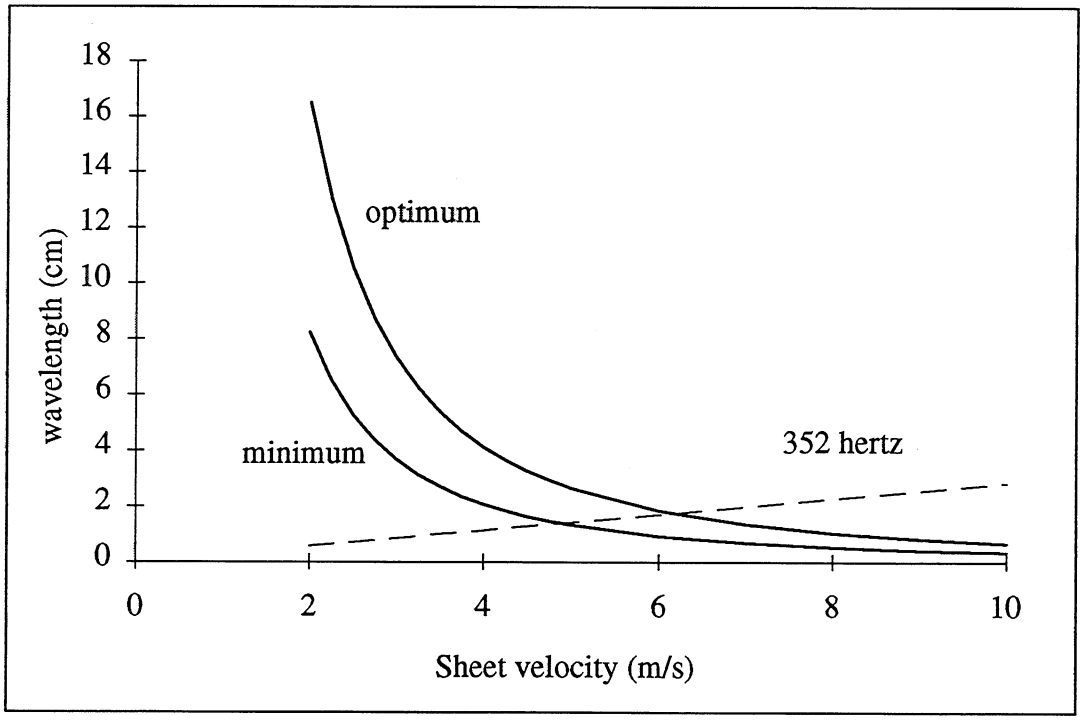

Figure 19. Optimum and minimum wavelength as a function of the sheet velocity - based on linear, inviscid theory.

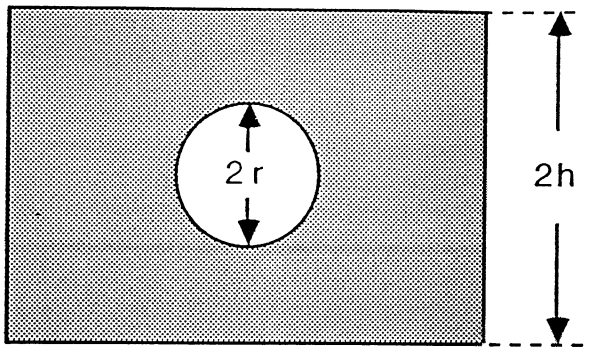

(a) the sheet thickness is much greater than the bubble diameter.

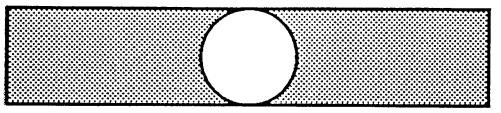

(b) the sheet thickness is on the order of the bubble diameter.

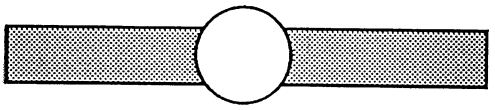

(c) the sheet thickness is less than the bubble diameter.

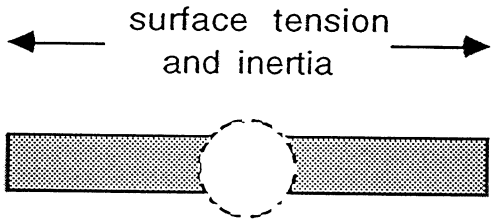

(d) bubble rupture and perforation growth.

Figure 20. Perforation initiation by an air bubble rupture mechanism.

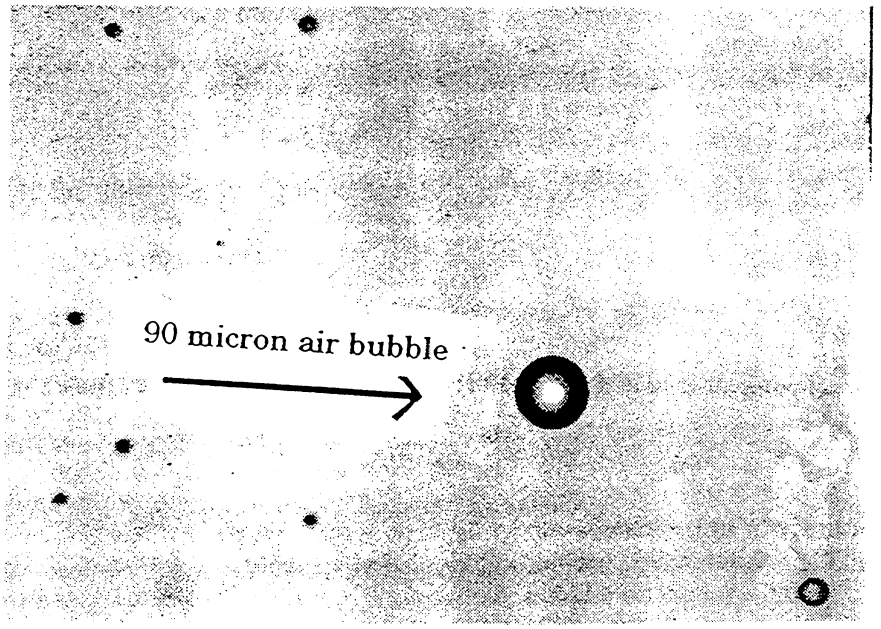

Figure 21. Typical entrained air bubbles (image at 200X magnification).

ACKNOWLEDGEMENT

Portions of this work were used by TMS as partial fulfillment of the requirement for the Ph.D. degree at the Institute of Paper Science and Technology.